Synthesis and characterization of caesium lead tri-iodide for solar cells

By
Sizwe Bhekithemba Sibiya

UNIVERSITEIT VAN PRETORIA
UNIVERSITY OF PRETORIA
YUNIBESITHI YA PRETORIA

Submitted in partial fulfilment of the requirements

for the degree

Magister Scientiae (MSc) in Physics

in the Faculty of Natural and Agricultural Sciences at the University of Pretoria

Supervisor: Prof. MM Diale

Co-Supervisor: Dr. N Nombona

March 2022

Declaration

I, SIZWE BHEKITHEMBA SIBIYA, declare that the dissertation, which I now submit for the degree, Masters (MSc) in Physics at the University of Pretoria, is my work and has not been submitted previously by me for a degree at this or any other institution. All sources or materials have been duly cited in the text, and a list of references is provided at the end of every chapter. Not a single part of the dissertation has been published in any of the journals thus far.

Signature……

Date…….

Student number: 12323277

Abstract

In this study, we report on the synthesis and characterization of titanium dioxide thin film prepared via the spray pyrolysis technique. X-ray diffractograms confirmed a tetragonal crystal structure with an average crystallite size of 24.44 nm and a micro-strain of $9.75x10^{-4}$. Field-emission scanning electron micrographs show pin-hole-free and densely packed grains with an average size ranging from 25 to 29 nm. UV-Vis spectra revealed an absorption onset of 300 nm for the film. The estimated film bandgap was 3.9 eV.

The sequential physical vapour deposition technique was used to grow quality thick films of metal halide perovskites in a safe, scalable, and reproducible manner. Growth of high-quality poly-crystalline yellow phase caesium lead tri-iodide ($CsPbI_3$) was refined by varying the CsI thickness from 200 nm to 500 nm. Crystallographic parameters and phase transitions from as-deposited orthorhombic γ-$CsPbI_3$ to tetragonal β-$CsPbI_3$ on annealing at 100 ℃, were determined using X-ray diffraction patterns. Computed lattice constants were a= 4.88 Å, b= 9.96 Å, and c= 16.52 Å, with an average crystallite size increasing from 169.46 nm to 243 nm, and the micro-strains decreased with an increase of CsI thickness. The field-emission scanning electron micrographs showed a uniform surface covered with polycrystalline grains. The Average grain size increased from 168 to 235 nm as the caesium iodide (CsI) thickness increased, resulting in large pin-hole-free and tightly packed grains. A 2.24 to 2.38 eV increase in the bandgap was observed when CsI thickness was increased. Herein, we demonstrated optimized structural, morphological, and optical properties of $CsPbI_3$ for use in solar cells, grown via sequential physical vapour deposition technique for stable and completely inorganic perovskites.

Finally, electrical properties of fabricated FTO/TiO_2/$CsPbI_3$/Au devices were characterized using the current-density (I-V) measurement technique. Although the CsI thickness varied, it had no effect on the cell's performance because the devices showed consistent power conversion efficiency of about 4%. Moreover, the open circuit voltage shows a decreasing trend when CsI thickness decreases.

List of abbreviations

AM	Air mass
BC	Back contact
CdS	Cadmium sulfide
CdTe	Cadmium telluride
CsI	Caesium iodide
$CsPbI_3$	Caesium lead tri-iodide
CB	Conduction band
CIGS	Copper indium gallium selenide
GaAs	Gallium arsenide
ETL	Electron transport layer
EPA	Environmental protection agency
FTO	Fluorine-doped tin oxide
GB	Grain boundary
HaP	Halide perovskites
HTL	Hole transport layer
HOMO	Highest occupied molecular orbital
ITO	Indium-doped tin oxide
LUMO	Lowest unoccupied molecular orbital
VB	Valence band
LED	Light-emitting diode
MABr	Methylammonium bromide

$MAPbBr_3$	Methylammonium lead tri-bromide
MAI	Methylammonium iodide
$MAPbI_3$	Methylammonium lead tri-iodide
PCE	Power conversion efficiency
PLQYs	Photoluminescence quantum yields
PV	Photovoltaic
SCLC	Space charge limited current
SPVD	Sequential physical vapour deposition
STVD	Sequential thermal vapour deposition
TWy	Terawatt year
WEO	World energy organization

Dedication

To my mother, Bettie J. Ntuli, and my little sister Sitholumusa S. Sibiya for their love, care, an insurmountable amount of support and prayers

&

To my lovely grandmother and late grandfather for their courageous consistent advices and their immense wisdom throughout my Bachelor's Degree

&

To Mphonyana Emily Thlathla for her endless love, care, courage, advice, and support

&

To my cousins Mandla R. Mahlangu, Michiel L. Mnisi,Goodboy R. Thombeni, Precious N. Jele, Gugukethu Kubheka, Valentine Jele, Mthokozisi M. Jele, Phindile Thombeni and the late Thandeka G. Thombeni for keeping me in their prayers.

&

To my fellow friends Musawenkosi S. Msibi, Tshepo A. Phola, William P. Seleka, and the late Zebulon F. Mpepele for their love, support, and belief in me.

Acknowledgment

Throughout my research, I appreciate the almighty God for providing me with wisdom, knowledge, understanding, safety, and health.

- I wish to express my deepest gratitude to **Prof. M Diale**, my supervisor, who deserves my appreciation for accepting to supervise me despite my lack of experimental experience and for transforming me from a mediocre scientific writer to an independent writer. Your motivation, difficult tasks, and thoughtfulness served as fuel for my research engine.
- I particularly like to Thank **Prof. David Cahen** for granting me access to his laboratories in the Weizmann Institute of Science and Bar Illan University, the knowledge, and training.
- I thank **Dr. N Nombona** for her guidance and granting me access to use the chemistry laboratory.
- I thank **Prof C.C. Theron,** Head of the Physics Department, for his support.
- To all the members of the **Clean and Green Energy Research group** at the University of Pretoria, I wish to show my gratitude to you all for the encouragement and friendship that countered the most challenging days and moments.
- I thank **Dr. Juvet N. Fru** for guiding me through my laboratory and proofreading my manuscript alongside **Dr. Justine Nyarige**. Thank you very much!
- I thank our collaborators in the Department of Chemistry at the University of Pretoria for UV-Vis absorption and XRD measurements. Sincere thanks to all the workers in the Laboratory for Microscopy and Microanalysis for their help.
- My heartfelt appreciation goes to my mother **Miss Bettie Judith Ntuli** who has been my pillar of strength through light and dark days. Thank you very much for being a candle of hope when no one believed in me and for all the sacrifices you've made for me until this day.
- I wish to extend the depth of my gratitude to my dear friends that I have started this journey with **Sandile Job Thubane, Thapelo Siemela,** and **Adiel Holtzhausen.**

- Thank you for all the wonderful memories that you allowed me to be a part of; thank you for all the love, care, courage, and support. **Mphonyana Emily Thlathla**.
- My sincere gratitude to the **National Research Foundation** (NRF) in South Africa, for making this golden opportunity possible. The University of Pretoria for provision of an enabling environment to play in research.

Table of Contents

List of Figures

List of Tables

1 Introduction

1.1 World energy demand and challenges

In recent years, global population growth and environmental factors, such as global climate change, have contributed to an upsurge in energy demand. A temperature reduction of 1°C during winter, for example, results in an additional 2.4 gigawatts of power demand throughout France [1]. According to the world energy organization (WEO) policy, the reported scenario in 2019, predicts that global energy demand is expected to nearly quadruple by 2050 [2]. Further predictions in *Figure 1.1* show a power model consumption presented by the Council for Scientific and Industrial Research (CSIR) for South Africa based on five scenarios of low to high electricity demand, from 2017 to 2049 [3]. The increasing energy demand at the moment is mostly met by non-renewable energy sources [4]. At present, fossil fuels such as coal, natural gas, and oil account for about 85% of global energy consumption [5]. Despite their enormous energy supply, we cannot ignore the looming issues of depletion of non-renewable resources and greenhouse gas emissions.

Non-renewable fossil fuels have led the world to several natural disasters including climate change and global warming. One of the world's most remarkable catastrophes has occurred due to global warming, including the destruction of polar bear habitats [6], ice-shelf melting around Antarctica [7], severe droughts [8], rising sea levels [9], and other extreme weather events. Global warming is known worldwide to have been potentially influenced by industrialization (during combustion of natural minerals) [10], global growth population [11], changing lifestyles [12], and consumerism. Burning natural minerals has become a major contributor to greenhouse gas emissions including methane (CH_4) [13], carbon dioxide (CO_2) [14], ozone (O_3) [15], and water vapour (H_2O) [16]. CO_2 is the most common greenhouse gas emitted by human activities in the United States. It accounted for about 35% to 70% of all greenhouse gas emissions reported by the United States Environmental Protection Agency (EPA) in 2019 [17]. Therefore, in order to mitigate CO_2 emissions in the atmosphere, most scientists and policymakers advocated for the replacement of fossil fuels as a means of supplying energy on a global scale [18]. Subsequently, over 192 nations 1997 signed the Kyoto protocol, [19], which was implemented in 2005 as a worldwide

deal to reduce greenhouse gas emissions. Then there was the 2015 Paris Agreement, which was signed by 195 countries. The Paris Accord marked a significant step forward in international climate cooperation. Its goal was to keep the world average air temperature rise below 2 ℃ before the end of the century, to decrease climate change's effects [20]. Instead of decreasing three years after the Paris Agreement, the percentage of CO_2 emissions climbed, following a three-year decline. More Intel for future forecasts indicates that the rate of increase will continue unless serious steps are made to ensure that the Paris accords are implemented globally [21].

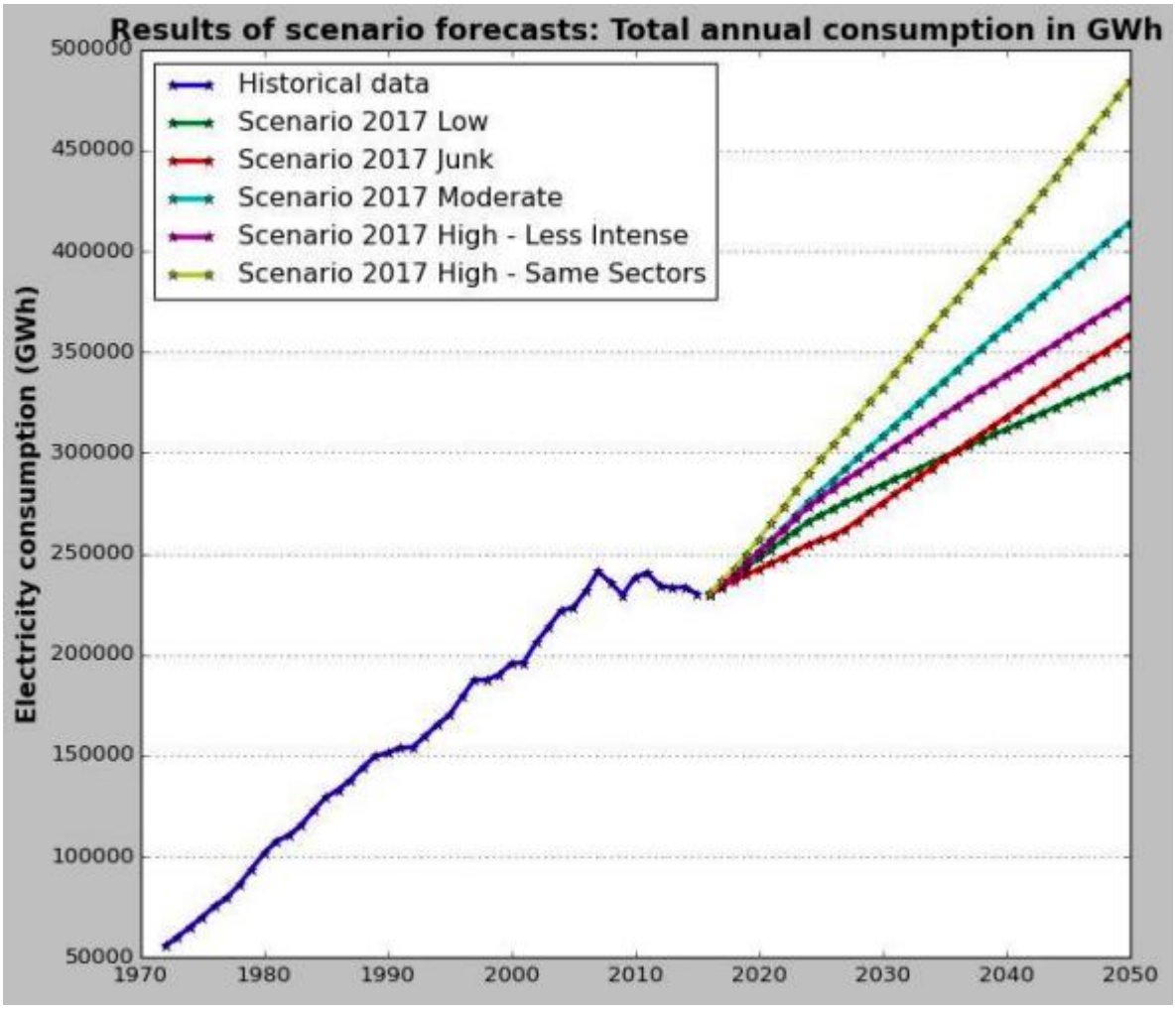

Figure 1.1: Developed CSIR electricity consumption model for South Africa from 2017 to 2049 [3].

Perez et al. [22] estimated the statistical value of solar energy to be 23,000 Terawatt year (TWy) and 14.72 TWy of non-renewable energy that is utilized per year. These resources will be depleted in the next 105 years (the year 2120). Shifting away from diminishing fossil fuels and toward renewable and green energy sources will prevent the future from energy depletion and frequent natural disasters. The green energy sources include biomass [23], wind [24], waves [25], geothermal [26], hydro [26] and solar [27]. Of all the renewable clean, and green energy sources listed, solar power generates only 8.76% of the world's electricity [28]. Furthermore, solar energy accounts for only 0.7% of worldwide energy consumption each year [29]. These findings lead to one conclusion: the solar power potential is underutilized, possibly because commercially available photovoltaic (PV) technology, like silicon, is too costly and inefficient [28].

Solar energy supply shows over 23,000 Terawatt year (TWy) is received by the Earth's crust yearly [30]. In 2015 global consumption of solar power was 18.5 TWy, far less than all other renewable sources shown in *Figure 1.2*. Additionally, *Figure 1.2* also shows that the total amount of nonrenewable energy reserved in 2015 was 1560 TWy. If the current 85% reliance on fossil fuels is maintained, while 14.72 TWy of the non-renewable energy is consumed, future projections illustrate full depletion of the nonrenewable resources (finite sources in *Figure 1.2*) in the next 105 years.

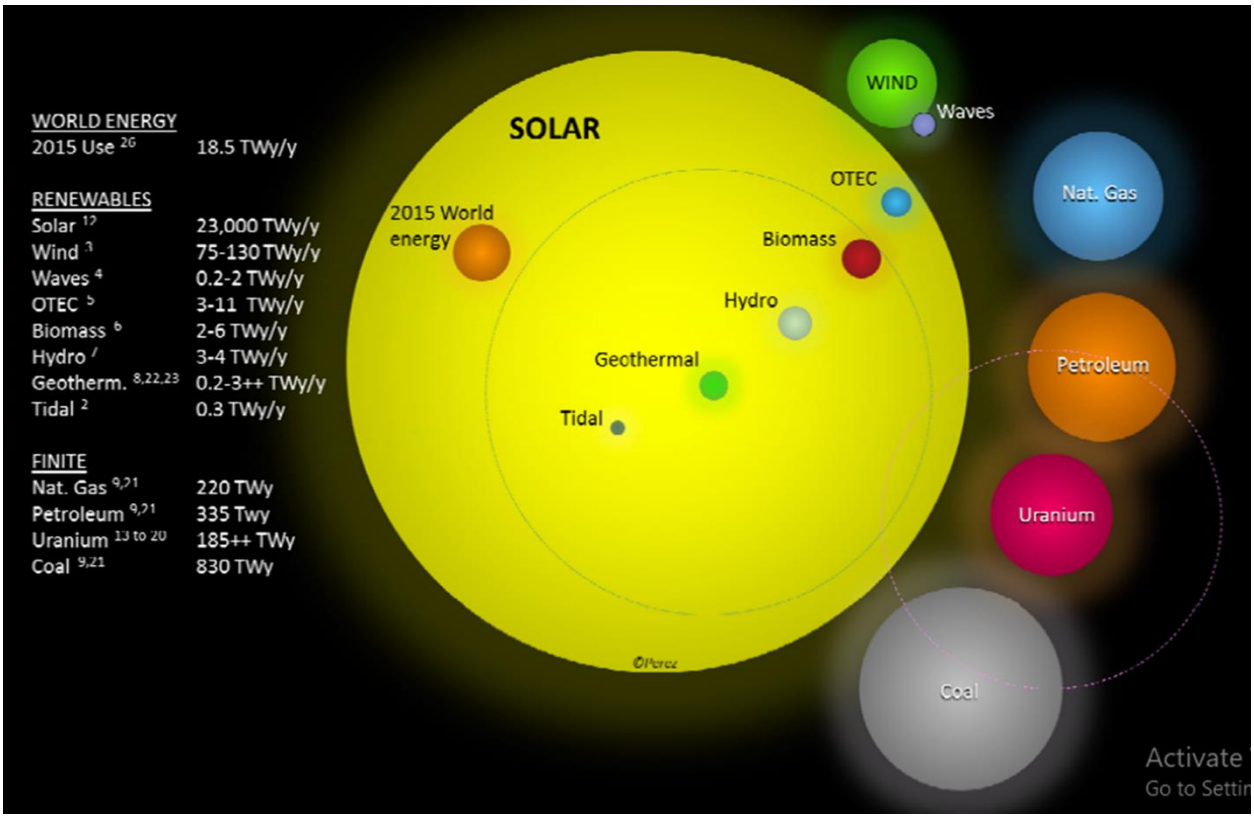

Figure 1.2: Reserves of finite and renewable energy in the world as of 2015 (Terawatt-years). For finite resources, total recoverable reserves are shown. Renewable energy potential is provided on a yearly basis [31].

Perovskite solar cells (PSCs) are considered part of the emerging photovoltaic (PV) technology in the third generation of light-harvesting materials [28], with great prospects for replacing the first (traditional Silicon-based) and second (traditional Cadmium Telluride/Cadmium Sulfide (CdTe/CdS)) generation photovoltaic solar cells currently available in the market [32]. Silicon-based (Si) solar cells, which have been studied for over 40 years, are among the most efficient PV devices. Due to Auger recombination, the efficiency of Si solar cells is limited to 29.4%, which is 4% less than the Shockley-Queisser (SQ) limit [33]. *Figure 1.3* shows the latest performance of various PV devices as they approach the SQ limit. The maximum theoretical solar cell efficiency measured under direct standard AM 1.5D spectral irradiance is 33.5% if measured by the SQ model [34]. On Earth, the solar spectrum is made up of two irradiance distributions.

Direct normal and hemispheric irradiance distributions of the sun (the blackbody) at 37º on a slanted surface are denoted as AM 1.5D and AM 1.5G, respectively [35]. In the direct standard, also known as the AM 1.5D spectrum of the blackbody, only direct sunlight is included. AM 1.5G, also known as the global standard, accounts for dispersed light emitted from the atmosphere. Shockley and Queisser assume a bandgap of 1.4 eV when applying an AM 1.5G solar spectrum to silicon (Si) and gallium arsenide (GaAs), which have band gaps of 1.12 eV and 1.42 eV, respectively, to maximize PCE of solar cells [34].

Even though Si-based PV technology is widely used, its PCE is only 26.7%, which is far below 33.5% of the SQ limit [34]. GaAs solar cells with 31% PCE are the only ones that come close to the SQ limit. Extrinsic and intrinsic constraints limit PV cells' ability to exceed the SQ limit. There are intrinsic limitations of PV, including (i) charge carrier depletion caused by high-energy photons exceeding the bandgap, (ii) losses due to radiative recombination, (iii) the direct bandgap of a PV material is desired for efficient absorption of high flux photons, and (iv) photons with energy below the bandgap are hard to absorb [36]. As a result, the extrinsic limitation is a function of the PV device's construction, so the design of the PV device leaves ample room for improving the extrinsic limitation [36]. Thus, research has focused on developing low-cost materials that can meet or exceed the SQ limit of GaAs and Si devices.

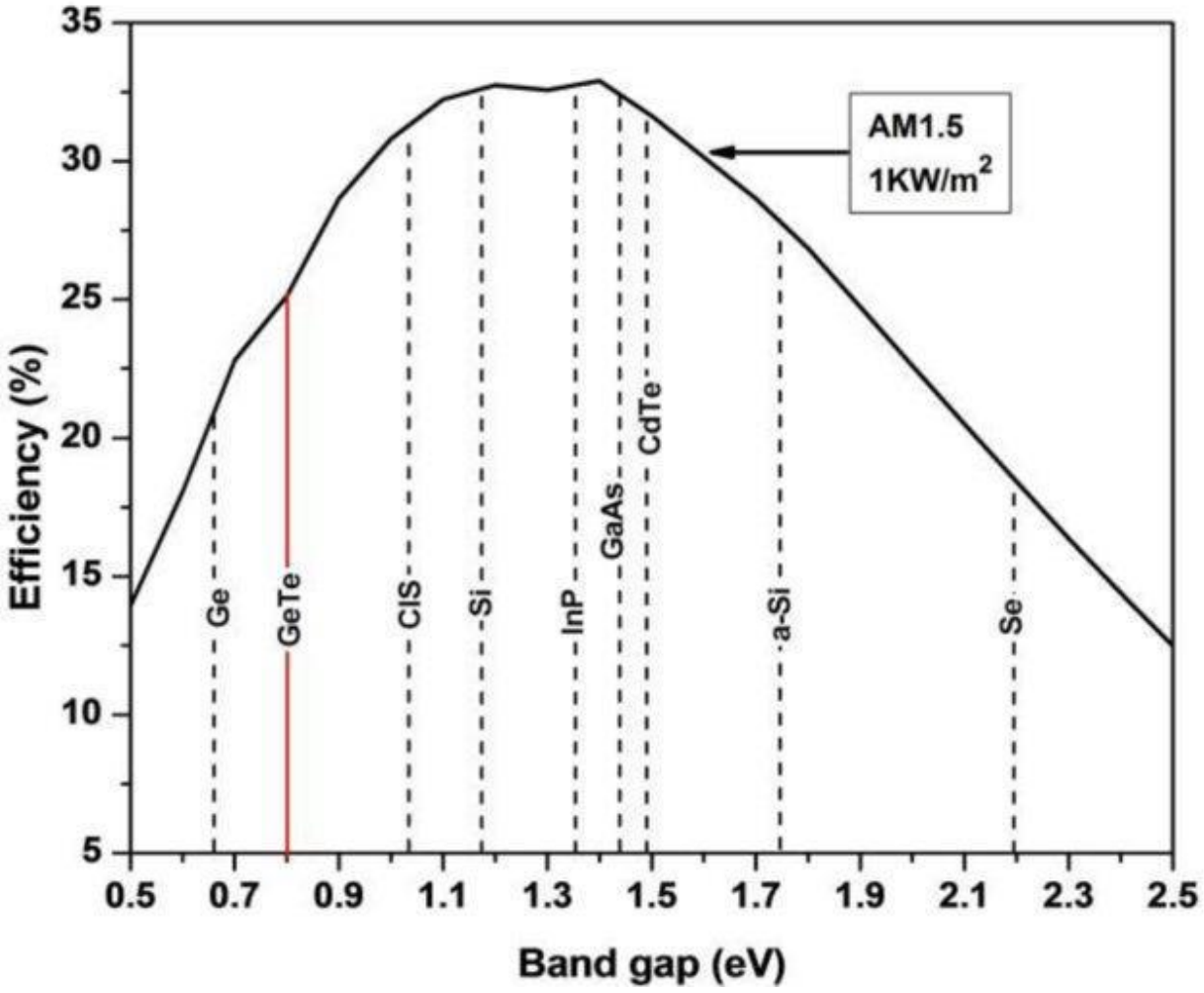

Figure 1.3: Shockley-Queisser efficiency (%) limit for p-n junctions as a function of the energy bandgap (eV) [37].

Over the last decade, perovskite-based solar cells (PSCs) have emerged as a promising solution to improve photovoltaic technology (both academically and industrially), by replacing the expensive first-generation PV devices based on Si, Gallium Arsenide (GaAs), and Copper Indium Gallium Selenide (CIGS). In a short period of time, the rapid growth of 3D metal halide PSCs PCE has surpassed that of well-studied organic photovoltaics (OPV), dye-sensitized solar cells (DSSCs). They are now being pushed to compete with well-established technologies such as Si wafers, GaAs, and CIGS [38]. As of now, several perovskite-based hybrid materials rank among the top 10 emerging technologies [39].

The first report based on $CH_3NH_3PbI_3$ ($MAPbI_3$) and $CH_3NH_3PbBr_3$ ($MAPbBr_3$) hybrid metal halide PSCs was reported by *Kojima et al.* [40] with the aid of enhancing DSSC's spectral absorbance in 2009. The reported FTO/m-TiO_2/DSSC/electrolytes/Pt device architecture demonstrated a PCE of 3.8%. Since late 2012, hybrid metal halides solar cells showed rapid growth reaching 25.5% PCE over 8years [41]. The National Renewable Energy Laboratory (NREL) presents in *Figure 1.4* the highest confirmed PCEs since 1976 for a range of PV technologies in research. NREL was founded in 1974 by the government of the United States. It focuses on renewable energy sources and their energy efficiency. According to the NREL presented growth trends in *Figure 1.4* of PCEs, perovskite-based solar cells have reached PCEs comparable to that of CdTe and CIGS single-junction solar cells (shown in the red circle).

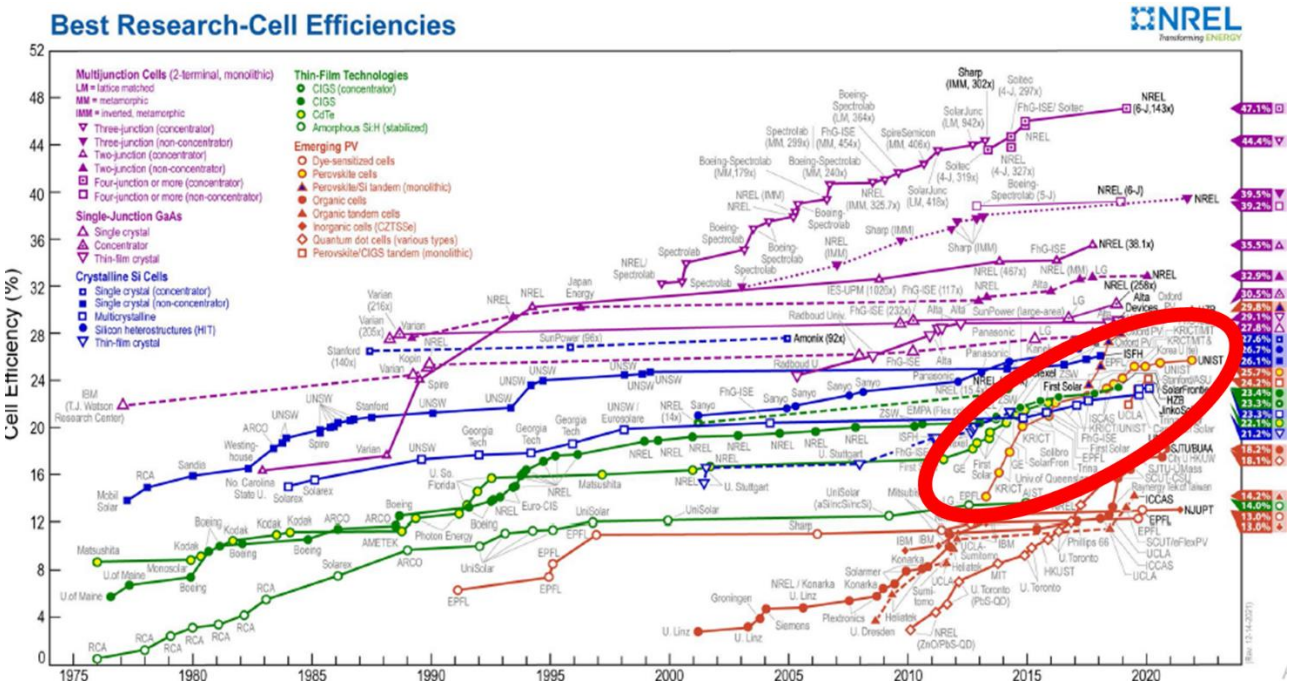

Figure 1.4: Displayed are the highest confirmed PCEs since 1976, for a range of PV technologies in research [42].

1.2 Challenges in the applications of perovskite-based devices

Despite the remarkable rapid growth of PSCs, pending challenges towards stabilization, upscaling for commercial use must be addressed before consideration for industrialization. The instability of PSCs is one of the major challenges, which limits their outside use. Extrinsic variables including humidity (due to the halides' affinity for H_2O) [43], photo-oxidation (due to O_2) [44], and ultraviolet (UV)-driven reactions all contribute to instantaneous device degradation in ambient conditions. Other variables limiting the perovskite-based devices include the lack of environmental [45] and functional stability [46], deficiency of reproducibility from laboratory-to-laboratory [47], the toxicity of lead, and other regularly used laboratory solvents [48]. Significantly the issue of reproducibility should therefore be addressed with an agency to ensure successful growth, stability, and long lifetimes in perovskite-based devices.

Techniques involving rate monitoring are not reproducible. Therefore, the purpose of this work is to resolve this challenge by examining the precursor's thickness to determine the film's stoichiometry. In order to optimize the stoichiometry, we use a crystal quartz monitor to determine the thickness of the precursor thin films. The technique ensures that high-quality perovskite-based films may be replicated from laboratory to laboratory.

1.3 Aims and objectives

This dissertation aims:

To verify the success of the sequential physical vapour deposition method for growing inorganic caesium lead tri-iodide thin films ($CsPbI_3$).

Following are the objectives:

i) The fabrication and characterization of spray pyrolysis deposited compact titanium dioxide (TiO_2) thin films.

ii) Optimize the structural, optical, morphological, and electrical properties of sequentially deposited thin films of $CsPbI_3$ by precisely monitoring the caesium iodide (CsI) thickness.

iii) Check for structural, optical, and morphological changes between as-deposited and post-treated thin films of $CsPbI_3$.

iv) The fabrication and characterization of $CsPbI_3$-based perovskite solar cells for various caesium iodide (CsI) thicknesses

1.4 Outline of the dissertation

The following five (5) chapters make up this dissertation.

Chapter 1 covers the introduction and motivation, background, and challenges in the applications of perovskite-based devices, as well as the aims and goal, and outline of the study.

Chapter 2 presents a literature review, as well as an overview of the structures and classes of metal halides and related solar cell models. The fundamentals of vacuum-assisted thermal deposition, growth, and performance of the devices.

Chapter 3 discusses the experimental techniques and characterization used in the study.

Chapter 4 presents the results of spray pyrolysis deposition of titanium dioxide and sequential physical vapour deposition of caesium lead tri-iodide thin films. The impact of varying CsI thickness on $CsPbI_3$ as-deposited and post-treatment (annealed) thin films.

Chapter 5 concludes and recommends possible future work.

1.5 References

1. Kim, H.-S., et al., *Lead iodide perovskite sensitized all-solid-state submicron thin film mesoscopic solar cell with efficiency exceeding 9%.* Scientific reports, 2012. **2**(1): p. 1-7.
2. Newell, R., D. Raimi, and G. Aldana, *Global energy outlook 2019: the next generation of energy.* Resources for the Future, 2019. **1**: p. 8-19.
3. Ma, Q., et al., *Hole transport layer free inorganic $CsPbIBr_2$ perovskite solar cell by dual source thermal evaporation.* Advanced energy materials, 2016. **6**(7): p. 1502202.

4. Mrabet, Z., et al., *Urbanization and non-renewable energy demand: A comparison of developed and emerging countries.* Energy, 2019. **170**: p. 832-839.
5. Bartok, W. and A.F. Sarofim, *Fossil fuel combustion: a source book.* 1991.
6. Thompson, R., W. Meyer, and B. Heitzinger, *Analysis of Polar Bear Protection Legislation.* 2007.
7. Rignot, E., et al., *Ice-shelf melting around Antarctica.* Science, 2013. **341**(6143): p. 266-270.
8. Feng, L., T. Li, and W. Yu, *Cause of severe droughts in Southwest China during 1951–2010.* Climate Dynamics, 2014. **43**(7): p. 2033-2042.
9. Tebaldi, C., et al., *Extreme sea levels at different global warming levels.* Nature Climate Change, 2021. **11**(9): p. 746-751.
10. Davidovits, J., *Global warming impact on the cement and aggregates industries.* World resource review, 1994. **6**(2): p. 263-278.
11. Molotoks, A., P. Smith, and T.P. Dawson, *Impacts of land use, population, and climate change on global food security.* Food and Energy Security, 2021. **10**(1): p. e261.
12. Whitmarsh, L., W. Poortinga, and S. Capstick, *Behaviour change to address climate change.* Current Opinion in Psychology, 2021. **42**: p. 76-81.
13. Hogan, K.B., J.S. Hoffman, and A.M. Thompson, *Methane on the greenhouse agenda.* Nature (London);(United Kingdom), 1991. **354**(6350).
14. Olivier, J.G. and J.A. Peters, *Trends in global CO_2 and total greenhouse gas emissions: 2017 report*. 2017: PBL Netherlands Environmental Assessment Agency The Hague.
15. Shindell, D.T. and G.A. Schmidt, *Southern Hemisphere climate response to ozone changes and greenhouse gas increases.* Geophysical Research Letters, 2004. **31**(18).
16. Berman, E.S., et al., *Greenhouse gas analyzer for measurements of carbon dioxide, methane, and water vapor aboard an unmanned aerial vehicle.* Sensors and Actuators B: Chemical, 2012. **169**: p. 128-135.
17. Mohlin, K., et al., *Turning the corner on US power sector CO_2 emissions—a 1990–2015 state level analysis.* Environmental Research Letters, 2019. **14**(8): p. 084049.
18. Burke, M.J. and J.C. Stephens, *Political power and renewable energy futures: A critical review.* Energy Research & Social Science, 2018. **35**: p. 78-93.

19. Nations, U., *Kyoto protocol to the United Nations framework kyoto protocol to the United Nations framework.* Rev. Eur. Community Int. Environ. Law, 1998. **7**: p. 214-217.
20. Falkner, R., *The Paris Agreement and the new logic of international climate politics.* International Affairs, 2016. **92**(5): p. 1107-1125.
21. Jackson, R., et al., *Persistent fossil fuel growth threatens the Paris Agreement and planetary health.* Environmental Research Letters, 2019. **14**(12): p. 121001.
22. Perez, R. and M. Perez, *A fundamental look at supply side energy reserves for the planet.* Int. Energy Agency SHC Program. Sol. Updat, 2015. **62**: p. 4-6.
23. Osman, A.I., et al., *Conversion of biomass to biofuels and life cycle assessment: a review.* Environmental Chemistry Letters, 2021. **19**(6): p. 4075-4118.
24. Abdel-Basset, M., et al., *A new hybrid multi-criteria decision-making approach for location selection of sustainable offshore wind energy stations: A case study.* Journal of Cleaner Production, 2021. **280**: p. 124462.
25. Chala, G.T., M. Ma'arof, and F.M. Guangul, *Tidal and Wave Energy Potential Assessment*, in *Clean Energy Opportunities in Tropical Countries*. 2021, Springer. p. 217-236.
26. Sayed, E.T., et al., *A critical review on environmental impacts of renewable energy systems and mitigation strategies: Wind, hydro, biomass and geothermal.* Science of the total environment, 2021. **766**: p. 144505.
27. Bhati, A., et al., *Solar Photovoltaic panels utilization to extract clean and green energy for utility application using PVsyst software: A Bibliometric Review.* Library Philosophy and Practice, 2021: p. 1-18.
28. Conibeer, G., *Third-generation photovoltaics.* Materials today, 2007. **10**(11): p. 42-50.
29. Fru, J.N., *Optimization of halide perovskite thin films by sequential physical vapour deposition for solar cell applications*, in *Physics*. 2020, University of Pretoria. p. 144.
30. Perez, M. and R. Perez, *Update 2015–a fundamental look at supply side energy reserves for the planet.* Natural Gas, 2015. **2**(9): p. 215.
31. Perez, R. and M. Perez, *A fundamental look at energy reserves for the planet.* 2009. **50**.
32. Park, N.-G., *Perovskite solar cells: an emerging photovoltaic technology.* Materials Today, 2015. **18**(2): p. 65-72.

33. Richter, A., M. Hermle, and S.W. Glunz, *Reassessment of the limiting efficiency for crystalline silicon solar cells.* IEEE journal of photovoltaics, 2013. **3**(4): p. 1184-1191.
34. Miller, O.D., E. Yablonovitch, and S.R. Kurtz, *Strong internal and external luminescence as solar cells approach the Shockley–Queisser limit.* IEEE Journal of Photovoltaics, 2012. **2**(3): p. 303-311.
35. Rühle, S., *Tabulated values of the Shockley–Queisser limit for single junction solar cells.* Solar energy, 2016. **130**: p. 139-147.
36. Boriskina, S.V. and G. Chen, *Exceeding the solar cell Shockley–Queisser limit via thermal up-conversion of low-energy photons.* Optics Communications, 2014. **314**: p. 71-78.
37. Al Noman, M.A., M. Abden, and M. Islam, *Germanium Telluride Absorber Layer, A Proposal for Low Illumination Photovoltaic Application Using AMPS 1D*. 2018.
38. Ono, L.K., E.J. Juarez-Perez, and Y. Qi, *Progress on Perovskite Materials and Solar Cells with Mixed Cations and Halide Anions.* ACS Appl Mater Interfaces, 2017. **9**(36): p. 30197-30246.
39. Kulbak, M., D. Cahen, and G. Hodes, *How important is the organic part of lead halide perovskite photovoltaic cells? Efficient $CsPbBr_3$ cells.* The journal of physical chemistry letters, 2015. **6**(13): p. 2452-2456.
40. Kojima, A., et al., *Organometal halide perovskites as visible-light sensitizers for photovoltaic cells.* Journal of the American Chemical Society, 2009. **131**(17): p. 6050-6051.
41. NREL, *Champion Photovoltaic Module Efficiency Chart.* 2020.
42. Socol, M. and N. Preda, *Hybrid Nanocomposite Thin Films for Photovoltaic Applications: A Review.* Nanomaterials, 2021. **11**: p. 1117.
43. Li, M., et al., *Recent progress on the stability of perovskite solar cells in a humid environment.* The Journal of Physical Chemistry C, 2020. **124**(50): p. 27251-27266.
44. Siegler, T., et al., *Water-Accelerated Photo-oxidation of CH3NH3PbI3 Perovskite: Mechanism, rate orders, and rate constants.* 2021.
45. Sidhik, S., et al., *Improving the stability of perovskite solar cells under harsh environmental conditions.* Solar Energy, 2020. **202**: p. 438-445.

46. Zhao, Y., et al., *Effects of ion migration and improvement strategies for the operational stability of perovskite solar cells.* Physical Chemistry Chemical Physics, 2021. **23**(1): p. 94-106.
47. Angmo, D., et al., *A lab-to-fab study toward roll-to-roll fabrication of reproducible perovskite solar cells under ambient room conditions.* Cell Reports Physical Science, 2021. **2**(1): p. 100293.
48. Kumar, A., et al., *Lead toxicity: health hazards, influence on food chain, and sustainable remediation approaches.* International journal of environmental research and public health, 2020. **17**(7): p. 2179.

2 Development of 3D halide perovskites for solar cells

2.1 Introduction

This chapter discusses the crystal structure, chemical formulae, and classification of halide perovskites (HaP) and related solar cell systems. A vacuum deposition of thin HaP films is introduced, as well as a variety of techniques for growing thin HaP films. It also discusses the evolution of photo-conversion efficiencies in HaP solar cells.

2.2 Crystal structure and chemical formula of HaP class

HaPs are composed of the AMX_3 compounds developed from calcium titanium trioxide ($CaTiO_3$), a natural mineral. The Russian mineralogist, Lev Alekseevich Perovski in 1839, first discovered this natural mineral. In the chemical formula AMX_3, A is a monovalent cation such as organic methylammonium (MA^+, $CH_3NH_3^+$), formamidinium (FA^+, $NH_2CH{=}NH_2^+$), and inorganic caesium (Cs^+), sodium (Na^+)or rubidium (Rb^+), B is a divalent metal cation such as lead (Pb_2^+), tin (Sn_2^+), and germanium (Ge_2^+)and X is a halide anion such as iodine (I^-), bromine (Br^-) or chlorine (Cl^-). It has a cubic crystal structure with the metal-cation at the 6-fold coordination position, surrounded by octahedron X-anions, called MX_6 octahedron framework, and the A-cation having 12-fold cuboctahedron coordination. The A-cation is larger than the M-cation, however, the size must fit into the 12-fold coordinated voids of the MX_6 octahedral inorganic framework, as shown in *Figure 2.1*. HaPs are capable of transitioning between cubic, tetragonal, and orthorhombic crystal polymorphs at a variety of temperatures [1]. This reversible transition depends on the ionic radius of the AMX_3 constituents.

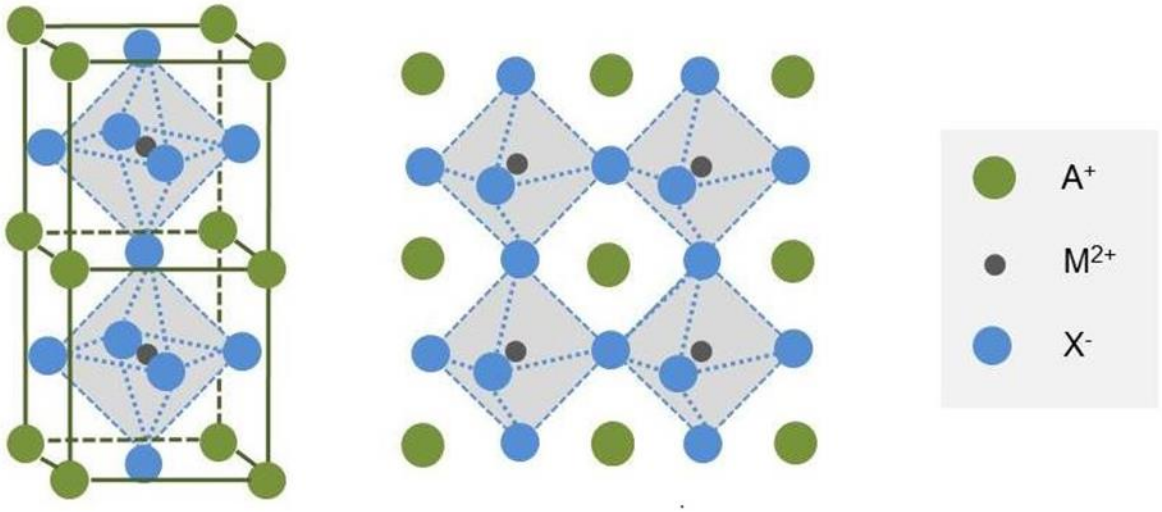

Figure 2.1: Cubic crystal structure of HaP with chemical formula AMX_3 [2].

The ionic radius of A-site cations contributes to the ability to form an ideal (cubic) AMX_3 HaP crystal structure. The tolerance factor increases with large-sized A-site ions. Both the Goldschmidt tolerance factor (TF) and octahedral factor (OF) help to predict the stability of the HaP based on the AMX_3 chemical formula [3]. The Goldschmidt TF is calculated using *Equation 2.1*:

$$TF = \frac{R_A + R_X}{\sqrt{2}(R_M + R_X)} \qquad \text{Equation 2.1}$$

where the ionic radii for A, B, and X sites are R_A, R_B, and R_X, respectively. A 3D HaP structure is inevitably stable when the TF is between 0.8 and 1[4]. The dimensionality of HaP crystals plays an integral role in the electrical, optical, and chemical properties, depending on the radius of the A-site cations and the voids generated by the MX_6 octahedral framework. It is possible to divide the intrinsic HaP crystal structure into four dimensions. According to *Figure 2.2*, these include three-dimensional (3D), two-dimensional (2D), quasi-2D, one-dimensional (1D) and zero-dimensional (0D). The morphology of the 3D structures is opal-like, maze-like, and coral-like [5].

In 2D HaP, four halides connect the $[PbI_6]^{4-}$ octahedron, forming a 2D network layer sandwiched between two organic layers. Furthermore, the layered structures have a nanoplatelet (nanosheet) perovskite and are separated by large organic spacer cations, comparable to the Ruddlesden-Popper (RP) phases [6]. The chemical formula of the 2D RP perovskites is denoted by A_2-$B_{n-1}M_nX_{3n+1}$, where A, B, M, and X are bulky organic spacer cations (such as phenyl-ethyl ammonium, PEA^+, and butyl ammonium, BA^+), monovalent cations (including Cs^+, MA^+), divalent metal cations (transitional metals such as Pb^{2+} and Sn^{2+}"), and halide anions (such as "I^-, Br^- and Cl^-"), respectively [7]. The *n* is the number of corner-sharing inorganics $[PbX_6]^{4-}$ octahedral layers between neighboring bulky organic spacers. Further, due to Van der Waals forces (between organic spacers and adjacent PbX_6 layers) and hydrogen bonds, 2D RP perovskites can retain their 2D structure unaltered [8]. As a result of their large band gaps and strong structural quantum confinement effect, 2D perovskites have a significant role in the application of light-harvesting, capping layers, passivation layers, and 3D interfacial layers [9].

The coordination of two opposite corners in a one-dimensional (1D) octahedron forms independent infinite chains. The crystal geometry of 1D perovskites nanowires and nanorods have a hexagonal phase with essential applications in light trapping and antireflection coating [10]. The quantum dots (0D) perovskites have very high photoluminescence quantum yields, approaching unity. In the quantum dot 0D analog, each $[PbI_6]^{4-}$ complex is neutralized with two or four cations (such as 2,2:6,2-terpyridine/Tpy) to form a molecule (such as, Tpy → $[Tpy]^{2+}$ + $[PbI_6]^{4-}$ = Tpy_2PbI_6) [11]. In addition, 0D quantum dots perovskites can emit light in the entire visible spectrum [12]. Furthermore, well-designed quantum dot HaP solar cells have high extinction coefficients and multiple excitons, leading to an increase in solar cell photo-conversion efficiency (PCE) [13].

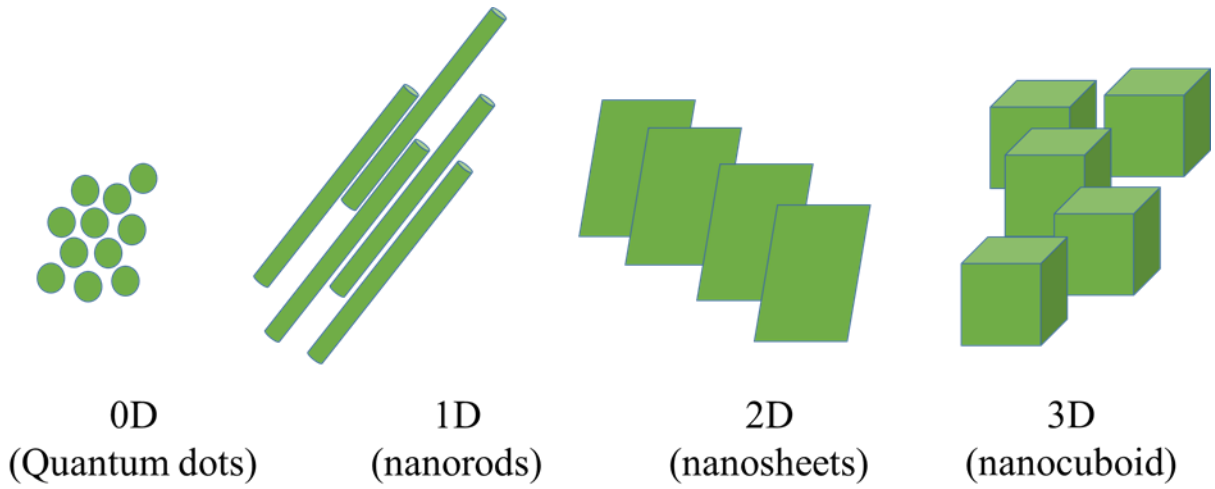

Figure 2.2: Structural dimensions of HaP.

2.3 Types of perovskites

2.4 Methylammonium lead tri-halide ($MAPbX_3$)

Electronic structure

Kim et al. [14] and *Baikie et al.* [15] determined the bandgap, valence band maximum (VBM), and conduction band minimum (CBM) of the material ($MAPbI_3$). The results of the Kuberlka-Munk transformed diffuse reflectance spectrum and ultraviolet photoelectron spectrum (UPS) indicated that the estimated bandgap, VBM, and CBM were 1.5, -5.43, -3.93 eV, respectively. *Yamada et al.* [16] used various optical techniques to engineer the optical response of $MAPbI_3$ on mesoporous titanium dioxide (TiO_2) electrodes, including PL, diffuse reflectance spectra, and transient absorption spectroscopy. $MAPbI_3$ grown on mesoporous TiO_2 was estimated to have a bandgap of 1.61 eV. *Schulz et al*. [17] used UPS and inverse photoemission spectroscopy (IPES) to investigate the $MAPbI_3$ interface energetics and electronic structure in solar cells. The results showed a larger electronic bandgap (1.7 eV) than the typical optical bandgap values for $MAPbI_3$ structures. Alternatively, the electronic structure of HaP was also studied using density functional theory (DFT). DFT calculations have demonstrated excellent agreement with

experimental measurements and can therefore be used to explain the excellent origins of halide perovskites' photovoltaic properties. *Wang et al.* performed the first DFT calculations of the $MAPbI_3$ electronic structure. According to the results, the experimental values were in good agreement with the measured bandgaps of 1.5 eV without taking spin-orbit coupling (SOC) into account [18]. *Even et al.* [19] later shed light on this unexpected agreement and revealed that the bandgap underestimation and neglecting the SOC in the DFT generalized gradient approximation (GGA) led to calculation errors. The study underscored the significance of using computational techniques to account for complex effects, including many-body effects, solid-organic-chemical interactions, and van der Waals interactions, in a lead-based organic-inorganic hybrid network to compute the electronic structure. There have been different computational techniques employed to study $MAPbI_3$ perovskites, such as PBE + SOC [19, 20], HSE + SOC [21] and GW + SOC [21, 22]. *Yin et al.* used the DFT-GGA technique to examine the cubic phase $MAPbI_3$ electronic structure, and the results obtained can help to explain the excellent optical and electrical properties of $MAPbI_3$ [17, 23]. The calculated density of states (DOS), band structure, and charge densities at VBM and CBM are displayed in *Figure 2.3*. The direct bandgap at R is 1.5 eV as shown in *Figure 2.3(a)*. Comparing the partial and total DOS (*Figure 2.3(b-e)*), we see that the CBM is dominated by Pb *p* orbitals in *Figure 2.3(f)*, while the VBM is dominated by I *p* states mixed with a negligible quantity of Pb *s* orbitals (*Figure 2.3(g)*). A direct bandgap p-p transition determines the optical transition of $MAPbI_3$, thus initiating strong optical absorption coefficients.

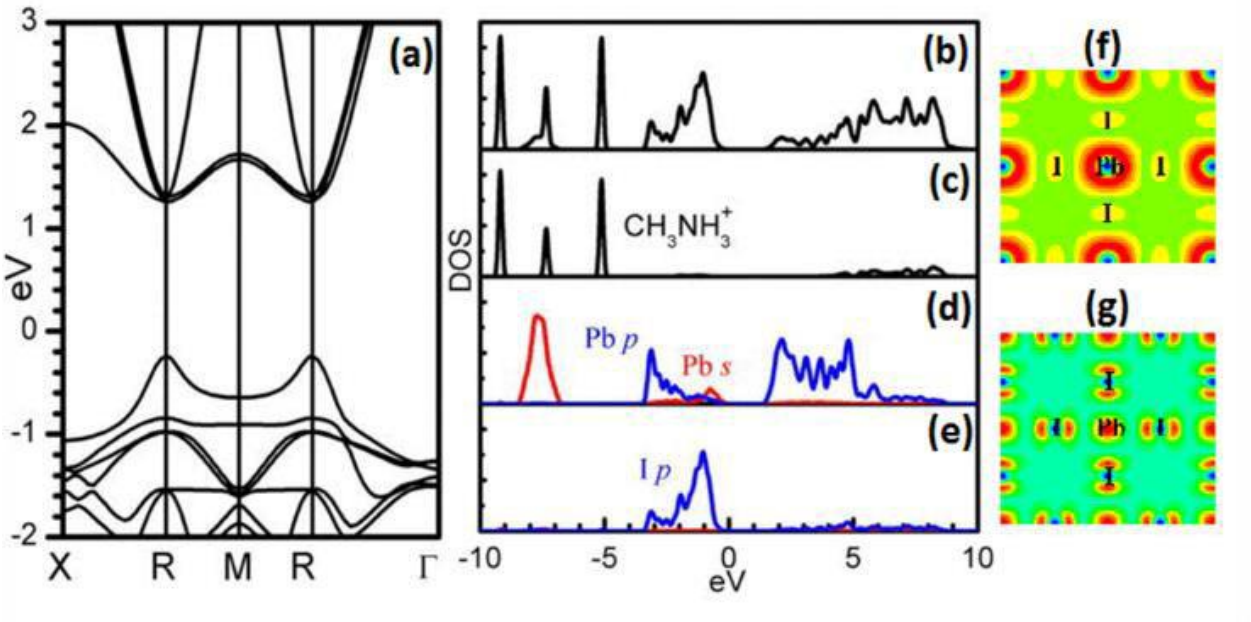

Figure 2.3: (a) Band structure; (b) total DOS; partial DOSs of (c) MA^+, (d) Pb, and (e) I; partial charge densities at (f) CBM and (g) VBM of $MAPbI_3$ [24].

Optical properties

A study conducted by *Papavassiliou et al.* [25] examined the optical absorption and photoluminescence spectra of Cs^+, $C_{10}H_{21}NH_3^+$, and $C_6H_5CH_2CH_2NH_3^+$ based compounds. As a result of grinding, the compounds displayed strong luminescence between 400 and 600 nm [25]. For photovoltaic applications, this feature is crucial for light absorption. The dielectric function of $CH_3NH_3PbI_{3-x}Cl_x$ and $MAPbI_3$ was later reported by *Yajie Jiang et.al* [26]. These results are comparable to traditional semiconductors showing low refractive indexes (2.10 - 2.25 at infrared wavelengths) and thus low absorption coefficients at above bandgap wavelengths, despite the high-band edge absorption [26]. The absorption coefficient of the ultra-thin $MAPbI_3$ perovskite film (obtained from optical transmittance measures and total reflectance measurements) was first reported by *Xing et al*. [27] in early solar cells using perovskites.

2.4.1 Formamidinium lead triiodide ($FAPbX_3$)

Electronic structure

Fan et al. [28] were the first to introduce the A-site cation-formamidinium (FA^+), achieving the formamidinium lead tri-iodide $FAPbI_3$ perovskite compound. They compared the perovskite's electronic properties with that of the traditional methylammonium lead tri-iodide ($MAPbI_3$). Theoretical calculations from the density functional theory (DFT) affirmed the octahedral tilting of $FAPbI_3$ to be smaller than of $MAPbI_3$ [29]. Moreover, *He et al.* [30] reported that $FAPbI_3$ has a weaker electron-photon coupling resembling its small free volume. Therefore results in longer carrier lifetimes. Furthermore, *Galkowski et al.* [31] revealed that $FAPbI_3$ has a lower effective mass than $MAPbI_3$, indicating that it has phenomenal semiconducting properties. Consequently, these outstanding properties (optimum bandgap and carrier transport) furnish $FAPbI_3$ as the most promising perovskite material for high-powered single-junction solar applications [32].

X-ray absorption near edge structure (XANES) is a flexible tool for investigating the electronic structure of materials, and it's been used to investigate the electronic structure of organic photovoltaics in the past [33]. This technique examines the local structure of FA molecules by selectively exciting nitrogen and carbon. *Shen et al.* [33] used nitrogen and carbon K-edge XANES technique and DFT to investigate the electronic structure of hexagonal $FAPbI_3$ films. They synthesized formamidinium iodide (FAI) powder from a mixture of 8.2 g HI (57 wt% in water, Alfa Aesar) and 3 g formamidine acetate ($CH_4N_2 \cdot C_2H_4O$) (99%, Aldrich). Equal amounts of FAI and PbI_2 were mixed in anhydrous DMF and later spin-coated on ITO/PEDOT: PSS film. Post annealing at 60 ℃ and 160 ℃ they achieved both yellow and black phase $FAPbI_3$ thin films, respectively. Herein, the bandgaps were obtained from XRD to be 1.59 eV which is in agreement with the theoretically calculated value of 1.62 eV [34]. In addition, they found that the C and N 2p states of FA hybridize with the Pb, I states at the conduction band minimum in hexagonal, but not perovskite, $FAPbI_3$.

Optical properties

According to the results of the structural analysis, the $FAPbI_3$ structure has a narrow bandgap between 1.43–1.48 eV, which may bring the efficiency of the $FAPbI_3$-based perovskite devices closer to the Shockley–Queisser (S-Q) limit [35]. Recent research from *Atourki et al.* [36] reported on $FAPbI_3$ doped with Li as a technique to enhance the optical properties of perovskites by reducing non-radiative combinations. Li n-type doping is said to prevent recombination through the production of free electrons. *Wang et al.* [37] demonstrate that the N-methyl pyrrolidone (NMP) technique reduced non-radiative recombination. Their approach uses NMP to synthesize smooth and highly crystalline FA-perovskite ($FAPbI_3$) films in ambient air.

The research revealed an alternate effective route that resulted in the synthesis of $FAI{\cdot}PbI_2{\cdot}NMP$ intermediate phase (produced during the film growth), which exhibited direct formation of the α-phase upon detaching and restricted the non-radiative recombination. With the improved high-quality optical properties, there was a PCE of 17.29% from air-processed FA-PSCs and a drop to 13.55% over 30 days of storage for unencapsulated cells.

2.4.2 Caesium Lead Triiodide ($CsPbX_3$)

Electronic structure

Perovskites based on $CsPbI_3$ have been known as a photoconductive material since 1958 [38], but they were only recently identified as a novel semiconductor material for photovoltaics [39] and light emission applications [40]. Ravi et al. demonstrated using DFT that anti-bonding hybridized Pb 6s and X (np) orbitals formed the VBM of $CsPbI_3$ hybrids perovskites, of which X (np) is dominant. However, Pb (6p) dominates the CBM, as shown in *Figure 2.4* [41]. Cs^+ does not affect the electronic properties of $CsPbI_3$ in comparison with the recognized organic A-site cations [42]. *Stoumpos et al.* [43] have validated that A-site cations can modify perovskite electronic properties indirectly due to Coulombic interactions and steric hindrance, resulting in crystal lattice distortion.

According to *Stoumpos et al.* [43], the effect changes the bandgap energetics near the band edges by restricting the electronic structure. Furthermore, *Zhizai Li* et al. [44], calculated the

electronic bandgaps of α-, β- and γ-$CsPbI_3$ structures. Tight-binding (TB) and DFT calculations of $CsPbI_3$ polymorphs revealed that the various bandgaps are direct [45], with the bandgap α-$CsPbI_3$ shifting from the R to Z and Γ in the Brillouin zone for β-$CsPbI_3$ and γ-$CsPbI_3$ respectively. *Zhizai Li et al.* [46], also found that the electronic bandgap increased gradually with the transition from α-$CsPbI_3$ to more distorted β- and γ-$CsPbI_3$ because the $[PbI_6]^{4-}$ rotations stabilize the top of VBM and destabilize the bottom of CBM. In comparison to $CsPbBr_3$ and $CsPbCl_3$, the large iodide radius of $CsPbI_3$ results in a notable change in the geometric and electronic structure [47].

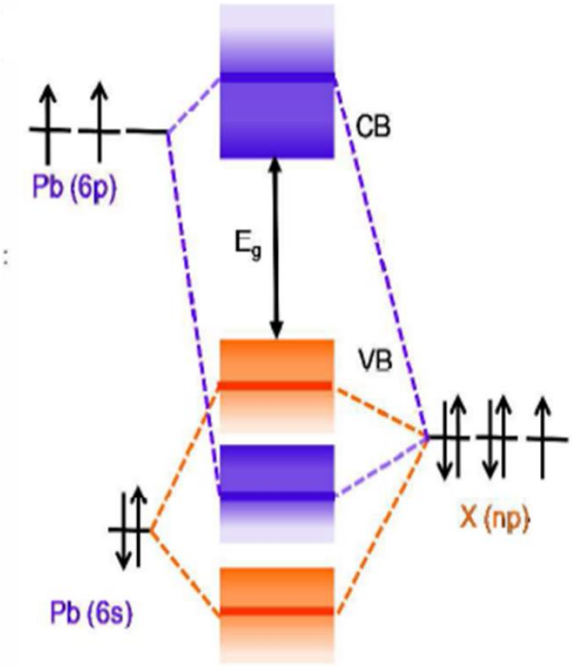

Figure 2.4: Electronic structure of $CsPbI_3$ for bonding and anti-bonding carriers [48].

Optical properties

Changing the size of all-inorganic metal halide perovskite (AIMHP) nanomaterials can change their bandgap and the optical absorption (emission). *Kovalenko et al.* [49] prepared $CsPbX_3$ materials that have incredibly tunable optical properties by reacting Cs-oleate with a Pb(II)-halide

in a high boiling solvent (octadecene) at 140−200 ℃, adding a 1:1 mixture of oleylamine and oleic acid are into octadecene to solubilize PbX_2 while stabilizing the colloidal nanocrystals. The tunable emission property of AIMHP nanomaterials makes them more attractive than other low-dimensional nanostructured materials, whose size, composition, and structure can be controlled.

These nanoparticles emit light with a range of wavelengths ranging from 400 nm (blue) to 700 nm (red), covering the entire visible spectrum of light [50]. *Zhang et al.* [51] have reported a direct method for the synthesis of high-quality 1-dimensional $CsPbI_3$ nanorods using solvothermal synthesis. Observed were high purity and uniform morphology, as well as ultrafine diameters of up to 5 nm. Photoluminescence quantum yields (PLQYs) and lifetime data indicate that nanorods exhibit a good surface state for a long time.

Phase stability

Nazeeruddin et al. prepared γ-$CsPbI_3$ thin films with no pinholes using a soft template-controlled technique. The template was adamantan-1-yl methanammonium (ADMA), which was ionized with hydro-iodide (HI). During $CsPbI_3$ formation, an induced steric effect resulted in an increased nucleation rate, while ADMA was absorbed by $CsPbI_3$. A PCE of 16.04% was reported based on the excellent morphology and controlling nucleation rate observed in Nazeeruddin et al.'s study. Aside from its controllable nucleation rate, γ-$CsPbI_3$ is a stable black phase due to its low dissociation energy [52]. In addition, *Hu et al.* [44] improved the material's stability by adding a small amount of water into a precursor to trigger a proton transfer process in $CsPbI_3$ films. A high-quality $CsPbI_3$ film was fabricated using HI and stored in ambient conditions without affecting performance, while the reference's PCE rapidly degraded.

$CsPbI_3$ has been found to be unstable due to its low Goldschmidt tolerance factor of 0.8472 and the strong interaction between the Cs^+ ion and $[PbX_6]^{-4}$ octahedron [53]. Strong ionic bonds cause crystal disorder and defects that result in phase transitions and poor efficiency. The polar solvents and moisture have also been found to adversely affect the $CsPbI_3$ [52]. A humid environment or polar solvents will cause the black phase to turn yellow if $CsPbI_3$ is exposed. *Kaiser et al.* [54] investigated the formation energies of the four phases as well as the reasons for

the better stability using the generalized gradient approximation (PBE) calculations. The results showed that due to the low formation energy of the γ-phase, it is the most stable phase structure in the black phases, while the stability of the β phase lies between the α-phase and the γ-phase.

Huang et al. also found that the γ-phase is the most stable in the black phase by using dissociation energy and density functional perturbation theory (DFPT), respectively [55, 56]. They found that the dissociation energies for α, δ, and γ-phase were 0.04, 0.09, and 0.16 eV, respectively, and affirmed that the lower the dissociation energy, the more stable the structure. As a result, the γ phase is more stable than the α-phase. *Even et al.* [69] confirmed the above statement by calculating the dispersion of phonons in the γ-phase without virtual modes at the G point and found no unstable phonons at any other high symmetry points [69]. Its energy, however, was the lowest, hence the conclusion above. ***Table 2.1*** shows configurations, methods of deposition, and annealing temperatures of various $CsPbI_3$-based perovskite solar cells.

Table 2.1. *Configurations, methods of deposition, and annealing temperatures of various $CsPbI_3$-based perovskite solar cells.*

Materials	Method	Configuration	Annealing temperature (°C)	Jsc [mA cm^{-2}]	Voc [V]	FF [%]	PCE [%]	Ref.
γ-$CsPbI_3$	Spin-Coating	FTO/TiO_2/$CsPb_{0.75}Ca_{0.25}I_3$/Spiro/Au	60	16.37	0.840	66.91	9.20	[57]
		FTO/TiO_2/$CsPbI_{2.85}Br_{0.15}$/PTAA/Au	-	19.75	1.135	76.60	17.1	[58]
		FTO/TiO_2/$CsPbI_3$:$Cl_{0.03}$/PTAA/Au	150	19.58	0.084	75.70	16.0	[59]

β-$CsPbI_3$	Spin-Coating	FTO/NiO_x/STCG-$CsPbI_3$/ZnO/ITO	100/150	17.40	1.020	79.40	14.1	[60]
		FTO/c-TiO_2/$CsPbI_3$/P3HT/Au	100/330	17.80	0.960	73.00	12.5	[61]

2.5 Preparation of HaP thin films

An interesting aspect of HaP preparation is the flexibility of the techniques, which can be broadly classified into solution and vapour techniques. Among the solution methods used for preparing HaP are ink-jet printing, gravure printing, doctor blades, electrode deposition, slot die casting, spin coating, and dip coating. Solution-based deposition techniques have been found to be economical, with low capital requirements, and fundamentally quick. Nonetheless, the requirements for quality control, solvent treatment, and dissolving solvents raise operating costs [62].

The spin coating process involves adding a solution to a horizontal spinning disk, which causes the solvent to evaporate, leaving a solid film as illustrated in *Figure 2.5*. There are a few sequential steps in this method, such as fluid dispensing, spinning up, stable fluid outflow, spinning off, and evaporation. Its extensive application in both research and industry makes it extremely valuable [63]. Using this fabrication process, perovskites can be grown over large surfaces (up to 30 cm) and have uniform and highly controllable film morphology [63]. In addition, the technique is capable of achieving desired film thicknesses for relevant sample sizes with ease [64]. The thickness of the film is determined by several variables, as shown in *Equation 2.2* below:

$$h = (1 - \frac{\rho A}{\rho_o} - \frac{3\eta \bullet m}{2\rho_{Ao}\ \omega^2})^{1/3} \qquad \text{Equation 2.2}$$

where h is thickness, ρ is the density of a volatile liquid, A is the surface area, η is the viscosity of the solution, m is the rate of evaporation, and ω is angular speed. Utilizing spin coating has the disadvantage of excessive material loss (over 90% of the deposited solution is wasted during deposition). It also has difficulties coating several films simultaneously, there is no control of contaminants (traces of oxygen, humidity), the coating lacks homogeneity [65, 66], and only works well for small substrate areas of less than 1.0 cm^2 [67]. Contrary to this, the technique has produced solar cells with very high PCE using a one-step [68] or two-step [69] depositions process. Prior to the deposition of a single-step film, the precursor solution is prepared in a suitable solvent(s). For two-step solution techniques, the lead halide or tin halide precursor is deposited sequentially with organic or caesium halide solution to form the perovskite. $FAPbI_3/MAPbI_3$ perovskite films, for example, are nucleated through a multicycle spin coating process. A PbI_2 layer is first deposited, then a solution of FAI/MAI with DMF solvent is added, which allows FAI/MAI to penetrate the PbI_2 framework to transform completely into perovskites.

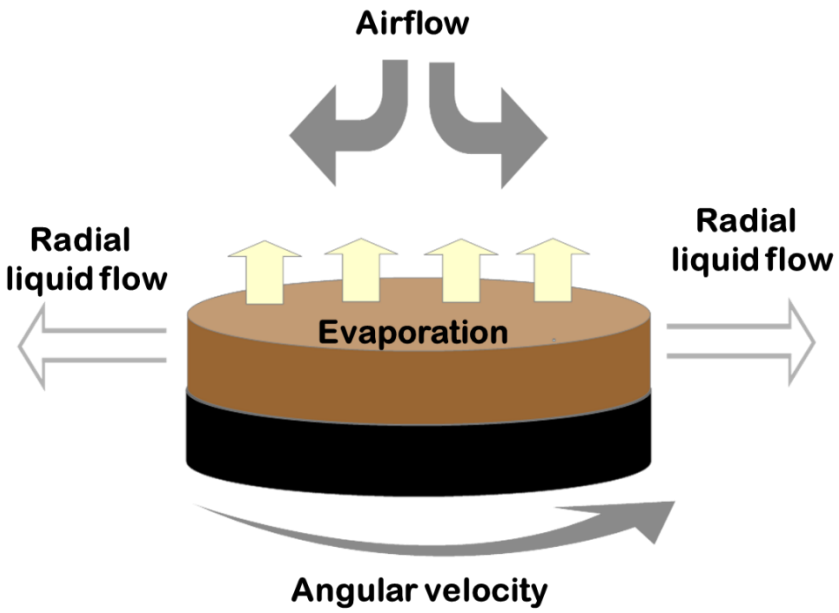

Figure 2.5: Diagram of a solution-based one-step spin-coating process for HaP thin-films fabrication.

On the other hand, vapour techniques are solvent-free, but require high capital investments and have a slow throughput. These techniques have been used for a wide range of applications, including the manufacture of solar cells [70]. Chemical vapour deposition (CVD) (shown in *Figure 2.6*), atomic layer deposition (ALD) [71], physical vapour deposition (PVD) [72], and sputter deposition [73] are common vapour techniques. In addition to being easy to control, these techniques provide stable laboratory-to-laboratory reproducibility without the need for treatment or recycling solvents. PV cells using the CVD technique produced thin films without pinholes, large grain sizes, good surface coverage, uniformity due to low defect density, and long carrier lifetimes. The CVD technique was used by *Wang et al.* [74] used the CVD technique under open-air conditions (ambient atmosphere with 40% humidity) and high deposition rates to produce films with increased carrier lifetime and high PCE. As of today, the technique has shown steadily rising PCEs.

Chen et al. [71] reported in early 2015 that their CVD technique produced PCEs between 12 and 15% and later reported a PCE of 17% [72]. *Chen et al.* [75] reported in early 2015 that their CVD technique produced PCEs between 12 and 15% and later reported a PCE of 17% [76]. In a recent study by *Qiu et al.* [77], CVD (compared with solution) technique was used to demonstrate a large-area, uniform coating of perovskite layers at a low cost. In addition, they revealed that the technique has more advantages including solvent-free, high compatibility with industrial manufacturing, and easy integration with other solar technologies to form tandem cells (or perovskite–perovskite tandem cells).

Another alternative is to use low-pressure chemical vapor deposition (LPCVD) [78]. ALD uses one or more volatile chemical precursors deposited on a substrate and then thermally reacting to deposit a thin solid coating. Unlike CVD, ALD is characterized by controlled, stepwise growth, allowing angstrom-scale control over film thickness as well as nanometric control over composition. To accomplish this, the film growth mechanism is split into self-limiting half-reactions, each involving only one of at least two precursors. A typical ALD cycle involves four steps: 1- The precursor A is pulsed into the reactor and chemisorbs onto the surface of the film. A single monolayer of a stable surface species is produced, and volatile by-products are generated. The excess precursor is unreactive with the surface it has formed. 2- To remove all unreacted

precursors, the reactor is purged with inert gas. Taking this step prevents the direct reaction of precursors A and B, which could result in uncontrolled CVD growth. 3- Monolayer A is reacted with precursor B in a self-limiting fashion to form a monolayer of the target film. The initial surface is regenerated, which allows precursor A to react in the next cycle. 4- Purging with inert gas.

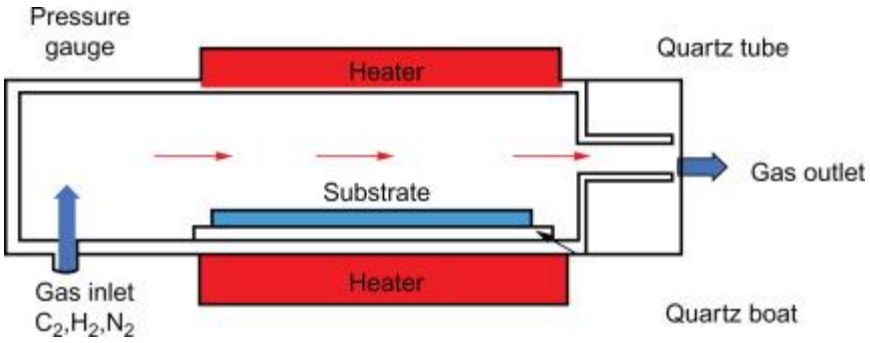

Figure 2.6: Chemical vapor deposition CVD for HaP fabrication [79].

A PVD process, on the other hand, involves converting solid-state material into thin films condensed under vacuum through the vapour phase. The PVD technique uses electrically resistive heating in conjunction with a high vapor pressure to perform a vaporization coating. The process is achieved in a vacuum chamber at a high vacuum (~10^{-6} torr). The process is divided into the following steps: heat is used to convert the material to be deposited into a vapor, the fluid is then transported from its source to a low-pressure region at the substrate, the vapor then condenses on the substrate to form a film, as shown in *Figure 2.7*. PVD is typically used to deposit films with thicknesses ranging from a few nanometers to thousands of nanometers. Films formed have improved properties, as well as the ability to deposit all types of inorganic materials and some types of organic materials be used. PVD is more environmentally friendly than spin coating.

Furthermore, sequential physical vapour deposition (SPVD) can be used to improve film reproducibility [80]. In this technique, gaseous precursors are sequentially applied to the substrate surface, as in *Figure 2.6*. For instance, *Ping Fan et al.* [81] have demonstrated a stoichiometric

excellent composition of $MAPbI_3$ perovskites with excellent thin-film properties. It had a high level of tetragonal phase purity, full surface coverage, well-defined grain structure, high crystallization, reproducibility, and a PCE of 10.90%. The SPVD process reduces contaminants by using vacuum while mitigating inhomogeneity, with the additional advantage of being able to fabricate more than two films at the same time [82]. The technique, however, has several downsides, including (i) difficulty coating complex shapes, (ii) high processing costs and low output, and (iii) process complexity [83].

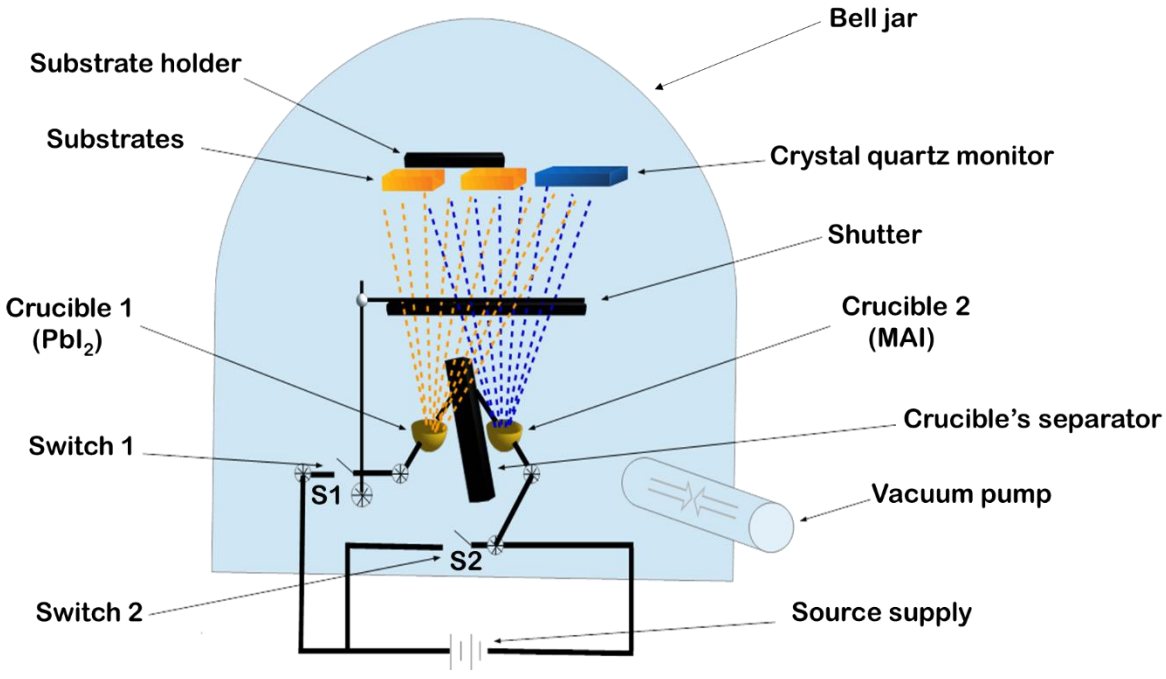

Figure 2.7: Simple structure of an SPVD technique [80].

2.6 Working principle of perovskite solar cells (PSCs)

A typical energy diagram of 3D halide PSCs is shown in *Figure 2.8*. The perovskites-based solar cell consisting of conventional/inverted architecture contains five components: cathode, hole transport layer (HTL), absorber layer (AL), an electron transport layer (ETL), and transparent conductive oxide. The perovskite AL is sandwiched in-between electron and hole transport materials. It absorbs incident light of wavelength equivalent to its bandgap for the generation of electron-hole pair (photoexcitation). The excited electrons are injected into the conduction band (CB) of the electron transport layer (TiO_2) and transported through the CB to reach the fluorine-doped tin oxide (FTO) substrate. From there it flows through the external circuit to the counter electrode (cathode), where it recombines with holes. Studies on perovskite devices with an insulating Al_2O_3 mesoporous layer [84, 85a], and even without any mesoporous layer (planar heterojunction with compact TiO_2 layer for collecting electrons), implied that electrons and holes can be transported through the perovskite film itself, without the need for any semiconducting scaffold as is required in the case of dye-sensitized solar cells. The slight variation in the device architecture concisely demonstrated that 3D halide PCSs operate analogous to the solid-state p-n junction solar cells, in discrepancy to the sensitization concept.

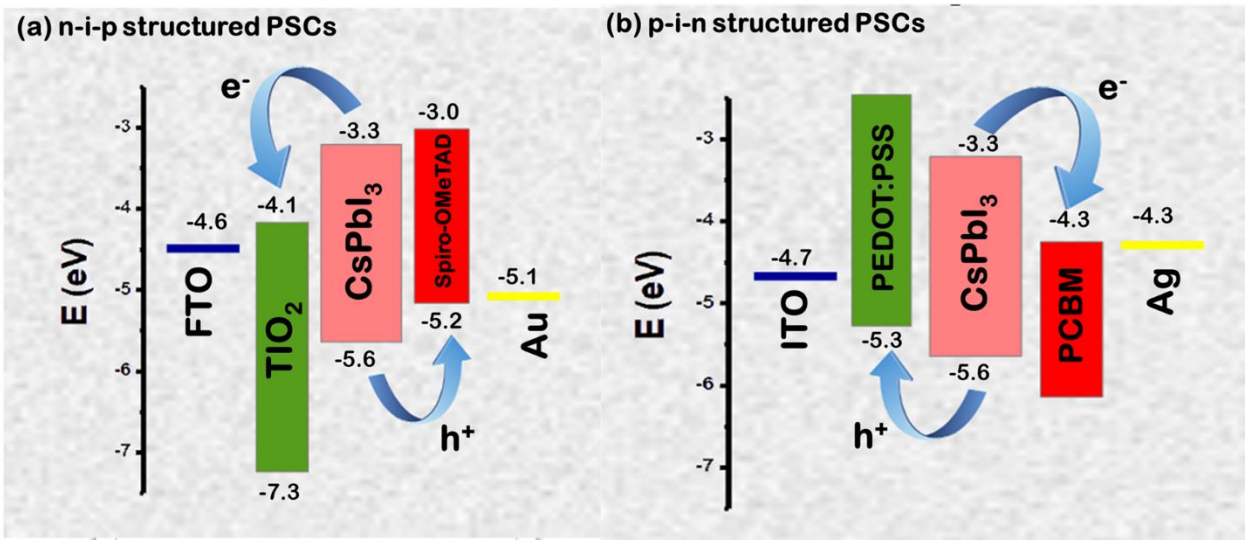

Figure 2.8: Energy diagram n-i-p and p-i-n HaP solar cells [85b].

.

2.7 Progress in photo conversion efficiency (PCE) of perovskite solar cells

Over the last decade, halide perovskite materials have revolutionized both academia and industry's approach to photovoltaic technology. They are currently vying to compete against established technologies based on silicon (Si) wafers, gallium arsenide (GaAs), and copper indium gallium selenide [86]. A study investigating hybrid 3D HaP ($MAPbI_3$ = $CH_3NH_3PbI_3$ and $MAPbBr_3$ = $CH_3NH_3PbBr_3$) reported in 2009 achieved a maximum efficiency of 3.8% [19], where the absorber was regarded as a dye-sensitizer deposited on TiO_2 [87]. Following an in-depth study, it was determined that the small PCE of the prototype devices was due to the rapid degradation (short stability) of the perovskite material caused by the liquid electrolyte hole transport material (HTM) [88]. This problem delayed the progress of PCE based on studies using $MAPbI_3$ and $MAPbBr_3$ hybrid perovskite materials for a short time. A remarkable open-circuit voltage (Voc) of 1 V was determined for the bromide perovskites. Scientists observed that the cells stopped functioning when acetonitrile was present in the perovskite. Due to the use of a nonpolar solvent-ethylacetate in place of acetonitrile, a PCE of 6.2% was achieved [89]. In addition, quantum dot-based cells showed excellent photovoltaic parameters and good stability. In the shortest amount of time in the history of PV technology, perovskite solar cells (PSCs) took an unprecedented leap. Halide perovskites have achieved PCEs of over 25.5% [90] to date.

Since the first report in 2015, the PCE of $CsPbX_3$-based PSCs has rapidly increased from 2.9% to 23.7% [91]. *Snaith et al.* [92] reported the first all-inorganic $CsPbI_3$ PSCs to have demonstrated a PCE of about 2.9% until 2015, using hydriodic acid (HI) inclusion to reduce its crystalline grain size. Later, *Luther et al.* [93], reported quantum dots-based solar cells for the *-$CsPbI_3$ that showed both improved PCE of over 10% and air-stability. *Luther et al.* found that the temperature phase transition of $CsPbI_3$ QDs was much lower than for their bulk counterparts. The QDs of the material ($CsPbI_3$) remained in their α-phase for a few more months at room temperature. Although the thermal stability of inorganic PSCs was greatly superior, their PCEs were still much lower than those of organic-inorganic PSCs.

Researchers since then have fabricated inorganic PSCs with high Voc, diminished energy losses, and short-circuit current density (Jsc), concentrating heavily on carrier extraction, transport, and optimized doping for $CsPbI_3$ to boost PCE. Using the MoO_3 hole transport layer, *Hayase et al.* [94] suppressed I–V hysteresis in a $CsPbI_3$ solar cell and showed a 4.68% PCE. Later on, *Ho-Baillie et al.* [95] introduced Br^- into *Snaith et al.'s* perovskite ($CsPbI_3$) to form $CsPbIBr_2$, thereby improving the phase stability. From a TiO_2/perovskite/Au architecture, the sample achieved a PCE of 4.7% (under reverse scan) post-annealing at 250 ℃ temperature. Secondly, *Ho-Baillie et al.* employed a two-step solution-assisted spray method to prepare $CsPbIBr_2$ films that had a stabilized PCE of 6.13% with negligible hysteresis [96]. The study examined the effect of annealing temperature on film quality and concluded that excellent crystallinity can be attained at temperatures that range from 275 ℃ to 350 ℃. The mesoporous structured devices produced by *Snaith et al.* [97] showed a 9.8% PCE and showed better stability than intrinsic $CsPbI_3$ perovskites. *Table 2.2* shows tabulated experimental conditions and photovoltaic PCEs of different all-inorganic α-$CsPbI_3$ perovskites with their solar cell structure

Table 2.2. *A summary of experimental environments and $CsPbX_3$-based device's performances.*

Perovskite materials	Configuration of PSCs	PCE (%)	Experimental environment	Ref.

$CsPbI_3$	ITO/PEDOT:PSS/P/PCBM/Al	0.09	–	[98]
$CsPbI_3$	ITO/PEDOT:PSS/P/PCBM/Al/Ca	2.9	N_2	[92]
$CsPbI_3$	FTO/bl-TiO_2/mp-	4.68	Atmosphere	[94]
$CsPbIBr_2$	TiO_2/P/P3HT/MoO_3/Au	4.7	N_2	[95]
$CsPbIBr_2$	FTO/c-TiO_2/P/Au	6.3	Atmosphere	[96]
$CsPbI_2Br$	FTO/c-TiO_2/mp-TiO_2/P/Spiro-MeOTAD/Au	9.8	Air-free	[97]
$CsPbBrI_2$	FTO/c-TiO_2/mp-TiO_2/P/Spiro-MeOTAD/Ag	6.8	Open-air	[99]
$CsPbI_3$	ITO/PEDOT:PSS/P/PCBM/BCP/Al	4.13	N_2	[100]
α-$CsPbI_3$ QDs	FTO/TiO_2/P/Spiro-MeOTAD/Ag	10.77	Atmosphere	[93]
$CsPbI_3$	FTO/TiO_2/PQDs/Spiro-	10.5	N_2	[101]
$CsPbI_2Br$	MeOTAD/MoO_x/Al	11.8	Atmosphere	[102]

2.8 References

1. Xiao, R., *Photocurrent Imaging of Single-Crystal Methylammonium Lead Iodide Nanostructures*. 2019, University of California, Davis.

2. https://www.surfacemeasurementsystems.com/effects-humidity-moisture-degradation-high-efficiency-perovskite-solar-cells/crystal-structure-of-perovskite compounds/#iLightbox[postimages]/3.

3. Bartel, C.J., et al., *New tolerance factor to predict the stability of perovskite oxides and halides.* Science advances, 2019. **5**(2): p. eaav0693.

4. Kieslich, G., S. Sun, and A.K. Cheetham, *Solid-state principles applied to organic–inorganic perovskites: new tricks for an old dog.* Chemical Science, 2014. **5**(12): p. 4712-4715.

5. Zhang, C., D.B. Kuang, and W.Q. Wu, *A review of diverse halide perovskite morphologies for efficient optoelectronic applications.* Small Methods, 2020. **4**(2): p. 1900662.

6. Popper, P., *The compound $Sr_3Ti_2O_7$ and its structure.* Acta Crystallogr, 1958. **11**: p. 54-55.

7. Mao, L., C.C. Stoumpos, and M.G. Kanatzidis, *Two-dimensional hybrid halide perovskites: principles and promises.* Journal of the American Chemical Society, 2018. **141**(3): p. 1171-1190.

8. Fu, P., et al., *Dion-Jacobson and Ruddlesden-Popper Double-Phase 2D Perovskites for Solar Cells.* Nano Energy, 2021: p. 106249.

9. Hanmandlu, C., et al., *Layered perovskite materials: key solutions for highly efficient and stable perovskite solar cells.* Reports on Progress in Physics, 2020. **83**(8): p. 086502.

10. Xue, P., et al., *Recent progress in molten salt synthesis of low-dimensional perovskite oxide nanostructures, structural characterization, properties, and functional applications: A review.* Journal of materials science & technology, 2018. **34**(6): p. 914-930.

11. Zhang, Y., et al., *Dimensionally and structurally controllable perovskite single crystals: nickel (ii)–terpyridine complex (Ni–Tpy 2)-based perovskites.* CrystEngComm, 2020. **22**(11): p. 1904-1908.

12. Li, Y.-F., J. Feng, and H.-B. Sun, *Perovskite quantum dots for light-emitting devices.* Nanoscale, 2019. **11**(41): p. 19119-19139.

13. Han, D., et al., *Efficient light-emitting diodes based on in situ fabricated $FAPbBr_3$ nanocrystals: the enhancing role of the ligand-assisted reprecipitation process.* ACS nano, 2018. **12**(8): p. 8808-8816.

14. Kim, H.-S., et al., *Lead iodide perovskite sensitized all-solid-state submicron thin film mesoscopic solar cell with efficiency exceeding 9%.* Scientific reports, 2012. **2**(1): p. 1-7.

15. Baikie, T., et al., *Synthesis and crystal chemistry of the hybrid perovskite $(CH_3NH_3)PbI_3$ for solid-state sensitised solar cell applications.* Journal of Materials Chemistry A, 2013. **1**(18): p. 5628-5641.

16. Yamada, Y., et al., *Near-band-edge optical responses of solution-processed organic–inorganic hybrid perovskite $CH_3NH_3PbI_3$ on mesoporous TiO_2 electrodes.* Applied Physics Express, 2014. **7**(3): p. 032302.

17. Schulz, P., et al., *Interface energetics in organo-metal halide perovskite-based photovoltaic cells.* Energy & Environmental Science, 2014. **7**(4): p. 1377-1381.

18. Wang, Y., et al., *Density functional theory analysis of structural and electronic properties of orthorhombic perovskite $CH_3NH_3PbI_3$.* Physical Chemistry Chemical Physics, 2013. **16**(4): p. 1424-1429.

19. Jishi, R.A., O.B. Ta, and A.A. Sharif, *Modeling of lead halide perovskites for photovoltaic applications.* The Journal of Physical Chemistry C, 2014. **118**(49): p. 28344-28349.

20. Lang, L., et al., *First-principles study on the electronic and optical properties of cubic ABX_3 halide perovskites.* Physics Letters A, 2014. **378**(3): p. 290-293.

21. Du, M.H., *Efficient carrier transport in halide perovskites: theoretical perspectives.* Journal of Materials Chemistry A, 2014. **2**(24): p. 9091-9098.

22. Brivio, F., et al., *Relativistic quasiparticle self-consistent electronic structure of hybrid halide perovskite photovoltaic absorbers.* Physical Review B, 2014. **89**(15): p. 155204.

23. Yin, W.J., T. Shi, and Y. Yan, *Unique properties of halide perovskites as possible origins of the superior solar cell performance.* Advanced Materials, 2014. **26**(27): p. 4653-4658.

24. Fan, Z., K. Sun, and J. Wang, *Perovskites for photovoltaics: a combined review of organic–inorganic halide perovskites and ferroelectric oxide perovskites.* Journal of Materials Chemistry A, 2015. **3**(37): p. 18809-18828.

25. *<papavassiliou2010.pdf>*.

26. Jiang, Y., et al., *Room temperature optical properties of organic–inorganic lead halide perovskites.* Solar Energy Materials and Solar Cells, 2015. **137**: p. 253-257.

27. Xing, G. and N. Mathews, *S, Sun, SS Lim, YM Lam, M. Grätzel, S. Mhaisalkar, and T. C. Sum.* Science, 2013. **342**(6156): p. 344-347.

28. Fan, Y., et al., *Review of Stability Enhancement for Formamidinium - Based Perovskites.* Solar Rrl, 2019. **3**(9): p. 1900215.

29. Mannino, G., et al., *Temperature-dependent optical band gap in $CsPbBr_3$, $MAPbBr_3$, and $FAPbBr_3$ single crystals.* The journal of physical chemistry letters, 2020. **11**(7): p. 2490-2496.

30. He, J., W.-H. Fang, and R. Long, *Unravelling the Effects of A-Site Cations on Nonradiative Electron–Hole Recombination in Lead Bromide Perovskites: Time-Domain ab Initio Analysis.* The journal of physical chemistry letters, 2018. **9**(17): p. 4834-4840.

31. Galkowski, K. and A. Mitioglu, *a. miyata, p. plochocka, o. Portugall, GE Eperon, JT-W. Wang, T. Stergiopoulos, SD Stranks, H. Snaith and RJ Nicholas.* Energy Environ. Sci, 2016. **9**: p. 962-970.

32. Jeon, N.J., et al., *A fluorene-terminated hole-transporting material for highly efficient and stable perovskite solar cells.* Nature Energy, 2018. **3**(8): p. 682-689.

33. Shen, P., et al., *Electronic structure of formamidinium ions in lead triiodide perovskites.* physica status solidi (RRL)–Rapid Research Letters, 2016. **10**(9): p. 677-681.

34. Lee, C., et al., *Organic–inorganic hybrid perovskites ABI 3 (A= CH_3NH_3, NH_2CHNH_2; B= Sn, Pb) as potential thermoelectric materials: a density functional evaluation.* Rsc Advances, 2015. **5**(96): p. 78701-78707.

35. Miller, O.D., E. Yablonovitch, and S.R. Kurtz, *Strong internal and external luminescence as solar cells approach the Shockley–Queisser limit.* IEEE Journal of Photovoltaics, 2012. **2**(3): p. 303-311.

36. Atourki, L., et al., *Impact of Li doping on the photophysical properties of perovskite absorber layer $FAPbI_3$.* Journal of Alloys and Compounds, 2021. **850**: p. 156696.

37. Wang, G., et al., *Fabrication of efficient formamidinium perovskite solar cells under ambient air via intermediate-modulated crystallization.* Solar Energy, 2019. **187**: p. 147-155.

38. Møller, C.K., *Crystal structure and photoconductivity of caesium plumbohalides.* Nature, 1958. **182**(4647): p. 1436-1436.

39. Protesescu, L., et al., *Nanocrystals of caesium lead halide perovskites ($CsPbX_3$, X= Cl, Br, and I): novel optoelectronic materials showing bright emission with wide color gamut.* Nano letters, 2015. **15**(6): p. 3692-3696.

40. Song, J., et al., *Nanocrystals: Quantum Dot Light - Emitting Diodes Based on Inorganic Perovskite Caesium Lead Halides ($CsPbX_3$)(Adv. Mater. 44/2015).* Advanced Materials, 2015. **27**(44): p. 7161-7161.

41. Ravi, V.K., G.B. Markad, and A. Nag, *Band edge energies and excitonic transition probabilities of colloidal $CsPbX_3$ (X= Cl, Br, I) perovskite nanocrystals.* ACS Energy Letters, 2016. **1**(4): p. 665-671.

42. Mangan, S.M., et al., *Dependence between Structural and Electronic Properties of $CsPbI_3$: Unsupervised Machine Learning of Nonadiabatic Molecular Dynamics.* The Journal of Physical Chemistry Letters, 2021. **12**(35): p. 8672-8678.

43. Stoumpos, C.C. and M.G. Kanatzidis, *The renaissance of halide perovskites and their evolution as emerging semiconductors.* Accounts of chemical research, 2015. **48**(10): p. 2791-2802.

44. Li, Z. and Z. Jin, *HI hydrolysis-derived intermediate as booster for $CsPbI_3$ perovskite: from crystal structure, film fabrication to device performance.* Journal of Semiconductors, 2020. **41**(5): p. 051202.

45. Ghaithan, H.M., et al., *Density functional study of cubic, tetragonal, and orthorhombic CsPbBr3 perovskite.* ACS omega, 2020. **5**(13): p. 7468-7480.

46. Katan, C., et al., *Interplay of spin–orbit coupling and lattice distortion in metal substituted 3D tri-chloride hybrid perovskites.* Journal of Materials Chemistry A, 2015. **3**(17): p. 9232-9240.

47. Li, X., et al., *All inorganic halide perovskites nanosystem: synthesis, structural features, optical properties and optoelectronic applications.* Small, 2017. **13**(9): p. 1603996.

48. He, X., Y. Qiu, and S. Yang, *Fully - inorganic trihalide perovskite nanocrystals: A new research frontier of optoelectronic materials.* Advanced Materials, 2017. **29**(32): p. 1700775.

49. Schlaus, A.P., et al., *How lasing happens in $CsPbBr_3$ perovskite nanowires.* Nature communications, 2019. **10**(1): p. 1-8.

50. Ha, S.-T., et al., *Metal halide perovskite nanomaterials: synthesis and applications.* Chemical science, 2017. **8**(4): p. 2522-2536.

51. Wen, Z., et al., *Controllable synthesis of $CsPbI_3$ nanorods with tunable photoluminescence emission.* RSC advances, 2019. **9**(43): p. 24928-24934.

52. Wu, T., et al., *Efficient and stable $CsPbI_3$ solar cells via regulating lattice distortion with surface organic terminal groups.* Advanced Materials, 2019. **31**(24): p. 1900605.

53. Lignos, I., et al., *Exploration of near-infrared-emissive colloidal multinary lead halide perovskite nanocrystals using an automated microfluidic platform.* ACS nano, 2018. **12**(6): p. 5504-5517.

54. Kaiser, W., et al., *First-Principles Molecular Dynamics in Metal-Halide Perovskites: Contrasting Generalized Gradient Approximation and Hybrid Functionals.* The Journal of Physical Chemistry Letters, 2021. **12**: p. 11886-11893.

55. Klarbring, J., *Low-energy paths for octahedral tilting in inorganic halide perovskites.* Physical Review B, 2019. **99**(10): p. 104105.

56. Marronnier, A., et al., *Anharmonicity and disorder in the black phases of caesium lead iodide used for stable inorganic perovskite solar cells.* ACS nano, 2018. **12**(4): p. 3477-3486.

57. Zhao, H., et al., *Preparation of Tortuous 3D γ - $CsPbI_3$ Films at Low Temperature by CaI_2 as Dopant for Highly Efficient Perovskite Solar Cells.* Advanced Functional Materials, 2019. **29**(27): p. 1808986.

58. Wang, H., et al., *Caesium lead mixed-halide perovskites for low-energy loss solar cells with efficiency beyond 17%.* Chemistry of Materials, 2019. **31**(16): p. 6231-6238.

59. Wang, K., et al., *Chlorine doping for black γ-$CsPbI_3$ solar cells with stabilized efficiency beyond 16%.* Nano Energy, 2019. **58**: p. 175-182.

60. Liu, C., et al., *Soft Template - Controlled Growth of High - Quality $CsPbI_3$ Films for Efficient and Stable Solar Cells.* Advanced Energy Materials, 2020. **10**(9): p. 1903751.

61. Lau, C.F.J., et al., *Fabrication of efficient and stable $CsPbI_3$ perovskite solar cells through cation exchange process.* Advanced Energy Materials, 2019. **9**(36): p. 1901685.

62. Smallwood, I.M., *Solvent recovery handbook*. 2002: CRC Press.

63. Liu, F.-K., et al., *Rapid fabrication of high quality self-assembled nanometer gold particles by spin coating method.* Microelectronic Engineering, 2003. **67**: p. 702-709.

64. Becker, W., et al., *Method and device for controlling thickness during spin coating*. 2004, Google Patents.

65. Chen, W.-F., P. Koshy, and C.C. Sorrell, *Effects of film topology and contamination as a function of thickness on the photo-induced hydrophilicity of transparent TiO_2 thin films*

deposited on glass substrates by spin coating. Journal of materials science, 2016. **51**(5): p. 2465-2480.

66. Krapf, L., et al., *AFM characterization of spin-coated multilayered dry lipid films prepared from aqueous vesicle suspensions.* Colloids and Surfaces B: Biointerfaces, 2011. **82**(1): p. 25-32.

67. Swartwout, R., M.T. Hoerantner, and V. Bulović, *Scalable deposition methods for large-area production of perovskite thin films.* Energy & Environmental Materials, 2019. **2**(2): p. 119-145.

68. Wang, G., et al., *Efficient perovskite solar cell fabricated in ambient air using one-step spin-coating.* RSC advances, 2016. **6**(49): p. 43299-43303.

69. Wu, J., et al., *DMF as an additive in a two-step spin-coating method for 20% conversion efficiency in perovskite solar cells.* ACS applied materials & interfaces, 2017. **9**(32): p. 26937-26947.

70. Fan, P., et al., *High-performance perovskite $CH_3NH_3PbI_3$ thin films for solar cells prepared by single-source physical vapour deposition.* Scientific reports, 2016. **6**(1): p. 1-9.

71. Antila, L.J., et al., *ALD grown aluminum oxide submonolayers in dye-sensitized solar cells: The effect on interfacial electron transfer and performance.* The Journal of Physical Chemistry C, 2011. **115**(33): p. 16720-16729.

72. Reichelt, K. and X. Jiang, *The preparation of thin films by physical vapour deposition methods.* Thin Solid Films, 1990. **191**(1): p. 91-126.

73. Compaan, A.D., et al., *High efficiency, magnetron sputtered CdS/CdTe solar cells.* Solar Energy, 2004. **77**(6): p. 815-822.

74. Wang, C., et al., *Air-induced high-quality $CH_3NH_3PbI_3$ thin film for efficient planar heterojunction perovskite solar cells.* The Journal of Physical Chemistry C, 2017. **121**(12): p. 6575-6580.

75. Chen, C.W., et al., *Efficient and uniform planar - type perovskite solar cells by simple sequential vacuum deposition.* Advanced Materials, 2014. **26**(38): p. 6647-6652.

76. Ng, A., et al., *Crystal engineering for low defect density and high efficiency hybrid chemical vapor deposition grown perovskite solar cells.* ACS applied materials & interfaces, 2016. **8**(48): p. 32805-32814.

77. Qiu, L., et al., *Metal Halide Perovskite Solar Cells by Chemical Vapor Deposition.* Journal of Materials Chemistry A, 2021.

78. Hoat, P.D., et al., *Synthesis of $Cs2SnI_6$ perovskite thin film by low-pressure chemical vapor deposition method.* Thin Solid Films, 2021: p. 138799.

79. Madhuri, K., *Thermal protection coatings of metal oxide powders*, in *Metal Oxide Powder Technologies*. 2020, Elsevier. p. 209-231.

80. Fru, J.N., *Optimization of halide perovskite thin films by sequential physical vapour deposition for solar cell applications*, in *Physics*. 2020, University of Pretoria. p. 144.

81. Fan, P., et al., *High-performance perovskite $CH_3NH_3PbI_3$ thin films for solar cells prepared by single-source physical vapour deposition.* Scientific reports, 2016. **6**: p. 29910.

82. Ohring, M., *The materials science of thin films.* Applied Optics, 1992. **31**(34): p. 7162.

83. Fru, J.N., N. Nombona, and M. Diale, *Characterization of sequential physical vapor deposited methylammonium lead tri-iodide perovskite thin films.* Vacuum, 2020. **182**: p. 109727.

84. Miyasaka, T., *Perovskite photovoltaics: rare functions of organo lead halide in solar cells and optoelectronic devices.* Chemistry Letters, 2015. **44**(6): p. 720-729.

85. (a) Lee, M.M., et al., *Efficient hybrid solar cells based on meso-superstructured organometal halide perovskites.* Science, 2012. **338**(6107): p. 643-647.

(b) Ma, T., et al., *The development of all-inorganic $CsPbX_3$ perovskite solar cells.* Journal of Materials Science, 2020. **55**(2): p. 464-479.

86. Ono, L.K., E.J. Juarez-Perez, and Y. Qi, *Progress on Perovskite Materials and Solar Cells with Mixed Cations and Halide Anions.* ACS Appl Mater Interfaces, 2017. **9**(36): p. 30197-30246.

87. Kojima, A., et al., *Organometal halide perovskites as visible-light sensitizers for photovoltaic cells.* Journal of the American Chemical Society, 2009. **131**(17): p. 6050-6051.

88. Snaith, H.J. and S. Lilliu, *The Path to Perovskite on Silicon PV.* Sci. Video Protoc, 2018. **1**(1).

89. Im, J.-H., et al., *6.5% efficient perovskite quantum-dot-sensitized solar cell.* Nanoscale, 2011. **3**(10): p. 4088-4093.

90. Green, M., et al., *Solar cell efficiency tables (version 57).* Progress in photovoltaics: research and applications, 2021. **29**(1): p. 3-15.

91. Kulbak, M., D. Cahen, and G. Hodes, *How important is the organic part of lead halide perovskite photovoltaic cells? Efficient $CsPbBr_3$ cells.* The journal of physical chemistry letters, 2015. **6**(13): p. 2452-2456.

92. Eperon, G.E., et al., *Inorganic caesium lead iodide perovskite solar cells.* Journal of Materials Chemistry A, 2015. **3**(39): p. 19688-19695.

93. Swarnkar, A., et al., *Quantum dot–induced phase stabilization of α-$CsPbI_3$ perovskite for high-efficiency photovoltaics.* Science, 2016. **354**(6308): p. 92-95.

94. Ripolles, T.S., et al., *Efficiency enhancement by changing perovskite crystal phase and adding a charge extraction interlayer in organic amine free-perovskite solar cells based on caesium.* Solar energy materials and solar cells, 2016. **144**: p. 532-536.

95. Ma, Q., et al., *Hole transport layer free inorganic $CsPbIBr_2$ perovskite solar cell by dual source thermal evaporation.* Advanced energy materials, 2016. **6**(7): p. 1502202.

96. Lau, C.F.J., et al., *$CsPbIBr_2$ perovskite solar cell by spray-assisted deposition.* ACS Energy Letters, 2016. **1**(3): p. 573-577.

97. Sutton, R.J., et al., *Bandgap - tunable caesium lead halide perovskites with high thermal stability for efficient solar cells.* Advanced Energy Materials, 2016. **6**(8): p. 1502458.

98. Choi, H., J. Jeong, and H. Kim, *B., Kim S., Walker B., Kim G.H., Kim JY.* Nano Energy, 2014. **7**: p. 80.

99. Beal, R.E., et al., *Caesium lead halide perovskites with improved stability for tandem solar cells.* The journal of physical chemistry letters, 2016. **7**(5): p. 746-751.

100. Luo, P., et al., *Solvent engineering for ambient-air-processed, phase-stable $CsPbI_3$ in perovskite solar cells.* The journal of physical chemistry letters, 2016. **7**(18): p. 3603-3608.

101. Frolova, L.A., et al., *Highly efficient all-inorganic planar heterojunction perovskite solar cells produced by thermal coevaporation of CsI and PbI_2.* The journal of physical chemistry letters, 2017. **8**(1): p. 67-72.

102. Chen, C.Y., et al., *All - Vacuum - Deposited Stoichiometrically Balanced Inorganic Caesium Lead Halide Perovskite Solar Cells with Stabilized Efficiency Exceeding 11%.* Advanced materials, 2017. **29**(12): p. 1605290.

3 Experimental

3.1 Introduction

The chapter lists the materials needed for the caesium lead tri-iodide ($CsPbI_3$) thin-film vapour deposition process. After describing the fluorine-doped tin oxide (FTO) substrate cleaning process, it provides a brief description of the sequenced physical vapour deposition of $CsPbI_3$. Furthermore, it reports on the characterization techniques such as x-ray diffraction (XRD), ultra-violet visible spectroscopy (UV-Vis), and scanning electron microscopy (SEM).

3.2 Materials

Table 3.1 lists the precursor chemicals. These chemicals were purchased from Sigma-Aldrich laboratories and they were used as received.

Table 3.1. *Concentration, purities, and the lists of precursors.*

Materials	**Purity/concentration**
Caesium lead iodide (CsI)	99.9%
Lead (II) iodide (PbI_2)	99.999%
Ethanol (Sigma–Aldrich Reagent)	N97%
titanium-tetra-isopropoxide (TTIP, Sigma-Aldrich)	99%

spiro-OMeTAD (Aldrich)	Anhydrous, 99.8%
chlorobenzene (CB, Aldrich)	≥99%
bis(trifluoromethylsulfonyl)-imide lithium salt (Li-TFSI, Aldrich)	99%
Tris(2-(1H-pyrazol-1-yl)-4-tert-butylpyridine) cobalt (III)-tris(bis(trifluoromethylsulfonyl)-imide) (FK209, Aldrich)	98%
4-tert-butylpyridine (TBP, Aldrich)	98%

3.3 Substrates and vacuum chamber cleaning procedure

This simple procedure was followed to remove contaminants such as dust particles, glass fragments (after trimming), grease, and oils from glass fluoride-doped tin oxide (FTO) transparent conductive substrates. The FTO/glasses were trimmed to size (1 cm x 1 cm) with a diamond cutter after sequentially dipping in acetone, isopropanol alcohol, and de-ionized water, each batch was sonicated for 10 min with a total sonication time of 30 min. A high-pressure nitrogen stream was used to dry the cleaned substrates. A diluted extra solution was used to clean the chamber before deposition. Cleaning both the chamber and substrates reduces the after-effects of the residual contaminants.

3.4 Preparation of compact titanium (II) oxide (c-TiO_2) thin films using the spray pyrolysis technique

The solution of compact-titanium dioxide (c-TiO_2) thin films were prepared from a mixture of 0.5M titanium tetra-isopropoxide (TTIP) (Sigma Aldrich, purity N97.0%), and 50 mL ethanol (Sigma-Aldrich Reagent) solutions. The mixture was stirred at room temperature (25 ℃) until it produced a colorless homogeneous solution. To keep some FTO areas free of c-TiO_2 coverage, the edge portions of the substrates were covered with thermal tape. Then, the substrates were placed on a hotplate. The hotplate was slowly warmed to prevent thermal strain on the glass substrates as the desired temperature of 250 ℃ was reached. The thin films were formed by spraying the c-TiO_2 solution mixture on the preheated substrates, using the spray pyrolysis technique, as illustrated in Figure 3.1. For this method, a spray pressure of 3 kPa was employed, air as a carrier gas, a 20 cm nozzle to substrate diameter and a 0.5 mm nozzle diameter, and with rapid sweeps, every 60 s and 15 s delays between them. Substrates were then allowed to cool to room temperature (25 ℃) naturally. Subsequently, c-TiO_2 thin films were annealed at 450 ℃ for an hour and characterized.

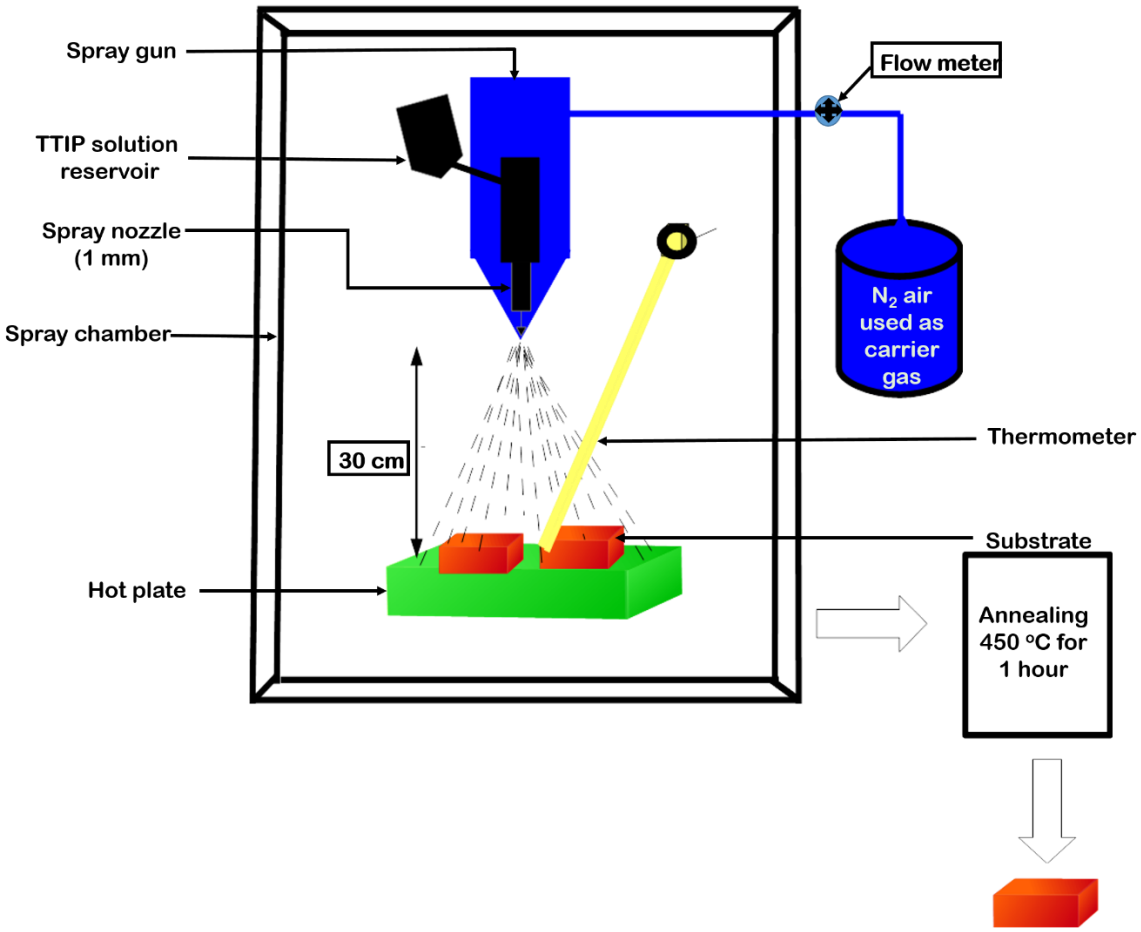

Figure 3.1: Schematic of spray pyrolysis.

3.5 Preparation of caesium lead tri-iodide ($CsPbI_3$) using the SPVD

Figure 3.2 displays the SPVD schematic for $CsPbI_3$.The thin films of $CsPbI_3$ were grown on cleaned and treated substrates (as described in section 3.3). CsI and PbI_2 precursors were used as received (from Sigma-Aldrich). Precursor powders were introduced into the chamber using separate boron nitride crucibles labelled C1 and C2, with C2 containing CsI and C1 containing PbI_2. The crucibles were placed on two separate heating coils for evaporation inside the chamber. The metallic coils were electrically separated by two switches S1 and S2 connected to an external power supply circuit, as illustrated in *Figure 3.2*. The turbo-pump was activated to exhaust air from the evaporation chamber until a vacuum pressure of 2×10^{-5} mBar was reached. With the aid

of a thermocouple and quartz crystal monitor, mounted on the same level as the substrates, the film temperature and thickness were constantly monitored. The monitor was set to have a Z-factor of 1.10 and a density of 6.16 g cm^{-3} for the PbI_2 powder. CsI thickness was also monitored with a calibrated crystal quartz monitor set with a Z-factor of 1.542 and density of 4.516 g cm^{-3} for the CsI powder. PbI_2 was evaporated when S1 is opened while S2 is closed, and vice versa for CsI. Once the required film thickness was achieved, the shutter was closed, and the current was gradually reduced to zero. Varying the PbI_2 and CsI thicknesses perfected the $CsPbI_3$ stoichiometry. The crystallization of $CsPbI_3$ was achieved by annealing the film at 100 ℃ for 10 minutes under an air-heated oven. Finally, using CsI (99, 9%) and PbI_2 (99, 9%), the experiment was repeated for varying thicknesses of CsI (from 200 nm – 500 nm) while PbI_2 is kept constant at 100 nm.

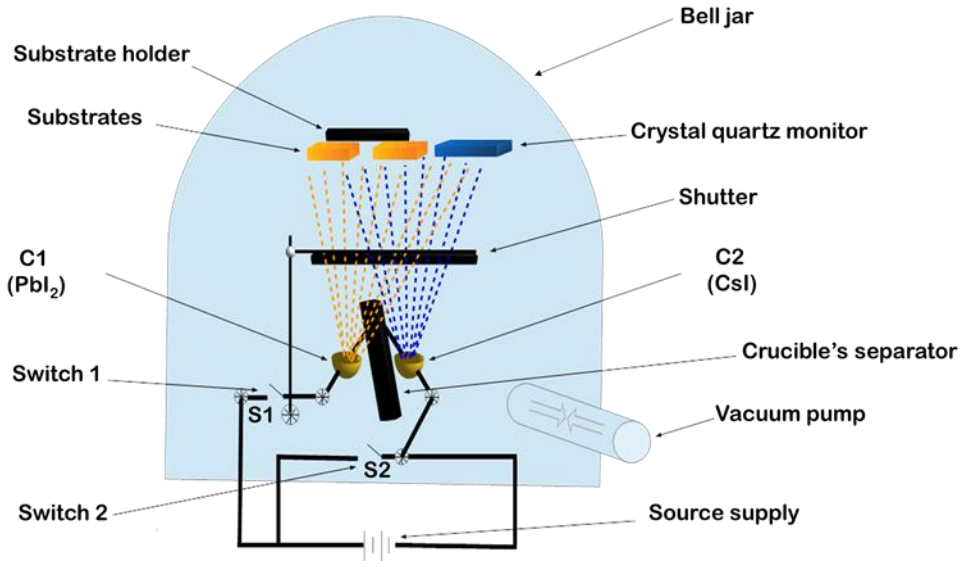

Figure 3.2: A schematic showing the growth of $CsPbI_3$ using the SPVD method.

3.5.1 X-ray diffraction for structural characterization

Figure 3.3 shows a schematic structure of an XRD setup. X-ray diffraction (XRD) is a rapid, non-destructive technique used to determine the molecular structure of natural and manufactured crystalline materials. The diffracted X-rays vary with the phase(s)/angle of a sample. Therefore, a comparison of the sample spectral pattern against a known reference sample in a search/match procedure provides the sample's phase(s). In addition, XRD methods are based on the scattering of X-rays by the atoms in a periodic array, that is, the lattice. Therefore positioning the sample and detector at locations in space with respect to the incident X-rays such that the diffraction maxima is detectable works the trick

Our thin films were examined using the Bruker D2-Phaser X-ray diffractometer after being exposed to Cu K radiation with a 1.5405 wavelength. From 10 to 50, 2θ was adjusted in 0.05 increments. A collimated monochromatic X-ray beam was directed at a rotating crystalline sample on the sample mount from the cathode source. The beam was diffracted by the crystal planes within the thin layer when it interacted with the sample, according to Bragg's law (*Equation 3.1*). Furthermore, the crystallite size, micro-strain, lattice constant, and dislocation density were all determined using diffractograms.

$$n\lambda = 2d\ sin\ \theta \qquad \text{Equation 3.1}$$

where n = 1, 2θ angle of Bragg's diffraction, λ is the beam's wavelength, and d is the distance between atom planes. The angle between the incident and diffraction beams 2θ is changed within a specified range (incident and the diffracted beams were varied from 20° to 80° with the step of 0.05 (2θ) and 4s per step) and diffractograms are recorded in a 2θ diffraction scan. *Equation 3.2* below was used to calculate the lattice constant of the orthorhombic annealed and as-deposited $CsPbI_3$ crystals.

$$\frac{1}{d^2} = \frac{h^2}{a^2} + \frac{k^2}{b^2} + \frac{l^2}{c^2}$$ Equation 3.2

Where a, b, and c are the lattice constants. The (hkl) parameters are the miller indices of the lattice plane system. Instrumental, crystallite size, and micro-strains are the three main factors that determine line broadening in diffractograms [1]. In addition, when the crystal lattice becomes defective, the X-ray diffraction peaks broaden [2]. We used the Williamson-Hall (WH) plot to determine the contributions of crystallite size and micro-strain to peak broadening [3], disregarding the instrument effect because it is systematic. Furthermore, Williamson and Hall's formula, given in *Equation 3.3*, defines the relationship between them.

$$FWHM \cos\theta = \frac{K\lambda}{D} + 4\mathcal{E} \sin\theta$$ Equation 3.3

where *FWHM* is the full width at half maximum of XRD determined from a Gaussian fit of peaks, used to characterize different material properties and surface integrity features, $\mathcal{E}$ is the micro-strain, θ is the Bragg angle, *D* is the crystallite size in the direction perpendicular to the lattice plane, λ is the wavelength of the X-rays, and *K* is a numerical factor (known as Scherrer constant) referred to as crystallite shape factor and consider as 0.94 for cubic symmetry with spherical crystallites. The micro-strain is presented by the slope of the W-H plot, and the crystallite size is equal to a constant multiplied by the reciprocal of the intercept shown by *Fru et al.* [4] in *Figure 3.4*. Furthermore, using Williamson and Smallman's equation (*Equation 3.4*), the crystallite size is related to the dislocation density ρ.

$$\rho = \frac{n}{D^2}$$ Equation 3.4

for the minimal dislocation density, n = unity.

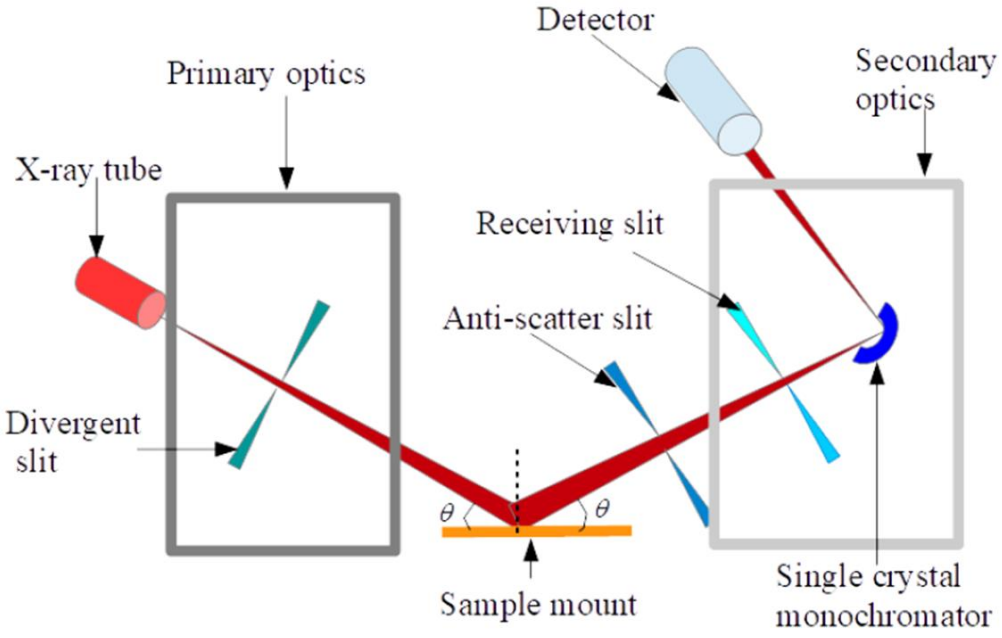

Figure 3.3: Schematic diagram showing the Bruker D2-Phaser X-ray diffractometer for XRD measurement process [5].

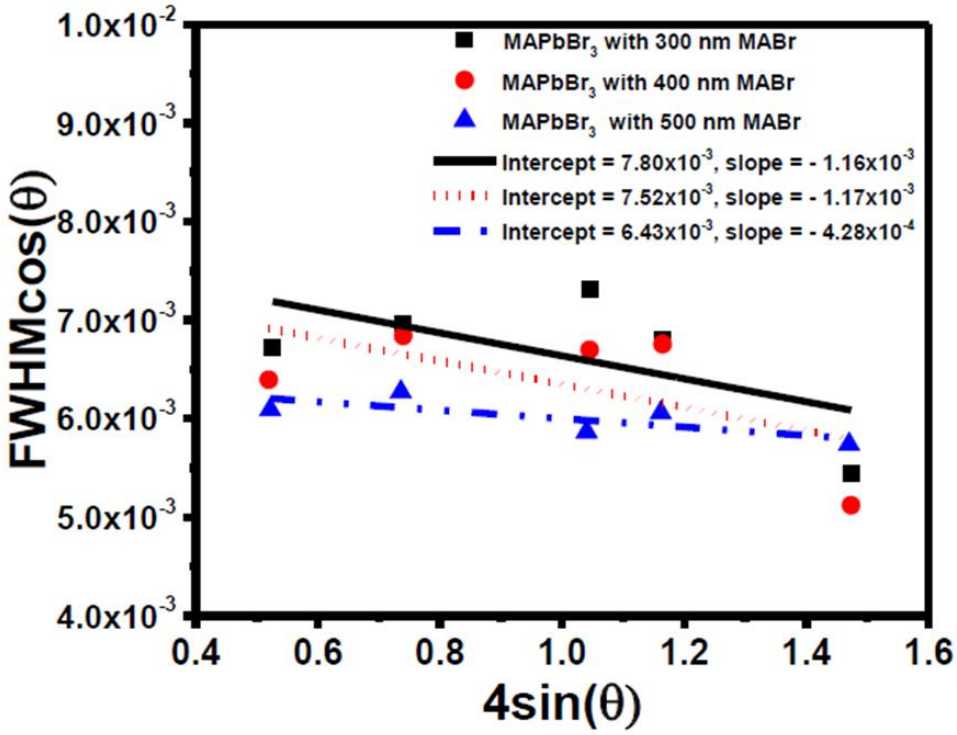

Figure 3.4: W-H plot of various thicknesses for $MAPbBr_3$ thin-films [4].

3.5.2 Scanning Electron Microscopy for Morphological Characterization

Scanning Electron Microscope (SEM) spectrometer is a destructive surface imaging technology that uses a beam of electrons (having high energy) in the range between (100-30,000 eV) to achieve a magnified 3D surface morphology and composition. SEM can scan particles as tiny as 10 nm. The instrument is composed of lenses that focuses the beam of electrons (from an electron gun) to the specimen under a vacuum path towards the anode as illustrated in *Figure 3.5*:. In addition, as the electromagnetic coil from above brings the beam into focus, the next electromagnet interacts (via electron beam) with the specimen side to side to generate a signal used to produce an image. The electrons that hit the surface are reflected, and the dispersed electrons are detected by the detector, resulting in data being converted into a picture. The constructed image is formed as the scan coils move around, as a result of the beam moving into discrete locations

until a rectangular raster appears on the specimen's surface in the shape of a straight line. The entire procedure is based on the desired magnification.

Herein, the morphology of the thin films was examined using a Field Emission Electron Microscopy (FE-SEM, Zeiss Crossbeam 540). The samples were deposited on Glass FTO as-deposited and annealed (100 ℃) before the analysis. Following the American Standard for Testing Materials (ASTM) we analyzed the grain size using the Image J software with the application of the Average Grain Intercept (AGI) concept.

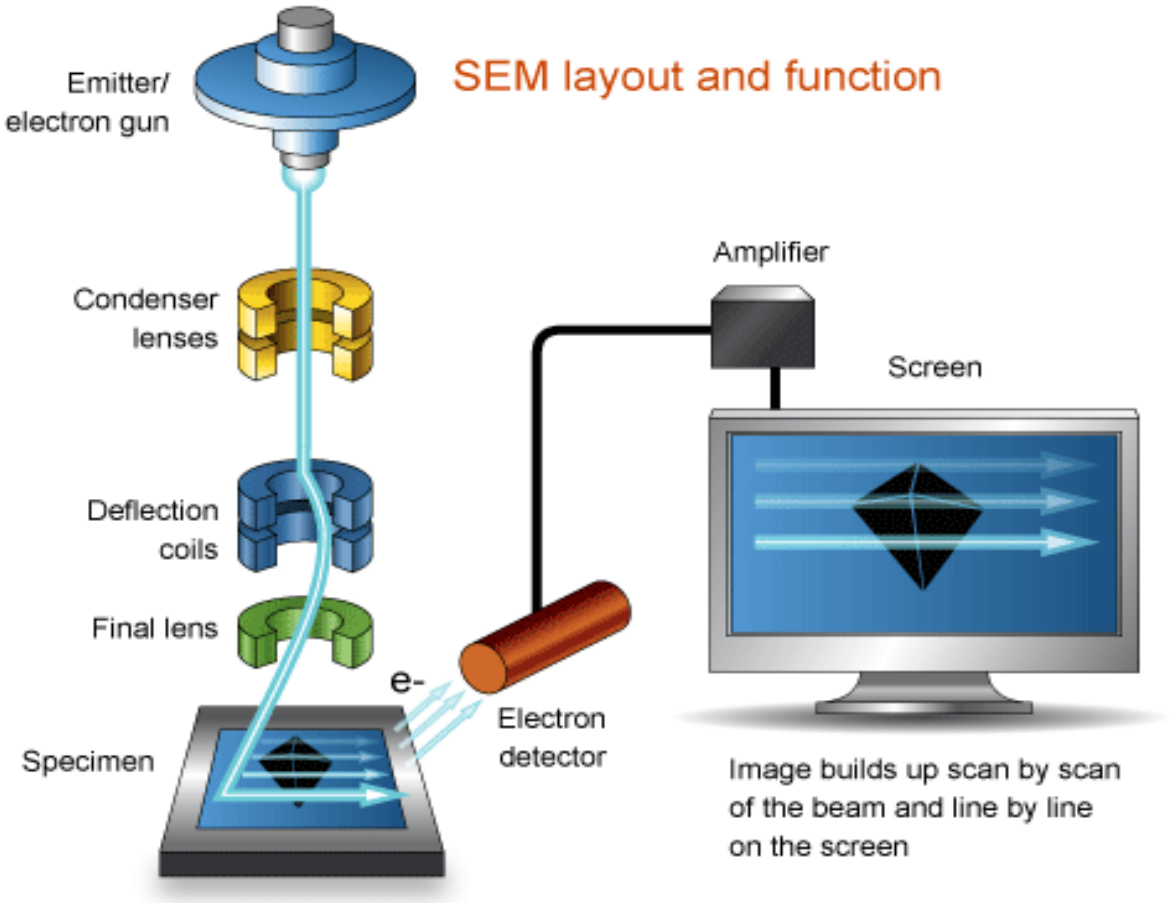

Figure 3.5: Display image of the components and working system of SEM during specimen analysis [6].

3.5.3 UV-vis spectrometer for Optical Absorption Spectrum

Figure 3.6 illustrates a simplified schematic diagram of the optical absorption spectrum measurement process using a UV-vis spectrometer. The phrase UV-vis Spectroscopy refers to the process of analysing various solvents and compounds. UV-vis spectrometers have been widely used for 37 years. Optical absorption spectra analysis is based on the detection of monochromatic light absorption in the near-ultraviolet spectrum (200 - 400 nm) by colourless compounds. This study used a CARY 100 BIO UV-vis spectrometer with incident light wavelengths ranging from 200 to 800 nm to observe the films' optical absorption spectra. The monochromator divides the light from the source into two beams, one of which travels through the sample and the other through the reference. The intensity of light traveling through the sample (*I*) is compared to that passing through the reference (I_o), which is equal to the intensity before light passes through the sample. The ratio (*I/Io*), which is related to absorbance in *Figure 3.5*, is known as the transmittance (%T).

$$A = -log(I/Io) \qquad \text{Equation 3.5}$$

Figure 3.6 shows the ratio, which is related to absorbance A, which is known as the transmittance (%T).

$$\alpha = 2.303(A/t) \qquad \text{Equation 3.6}$$

where the parameter t is the thin film thickness.

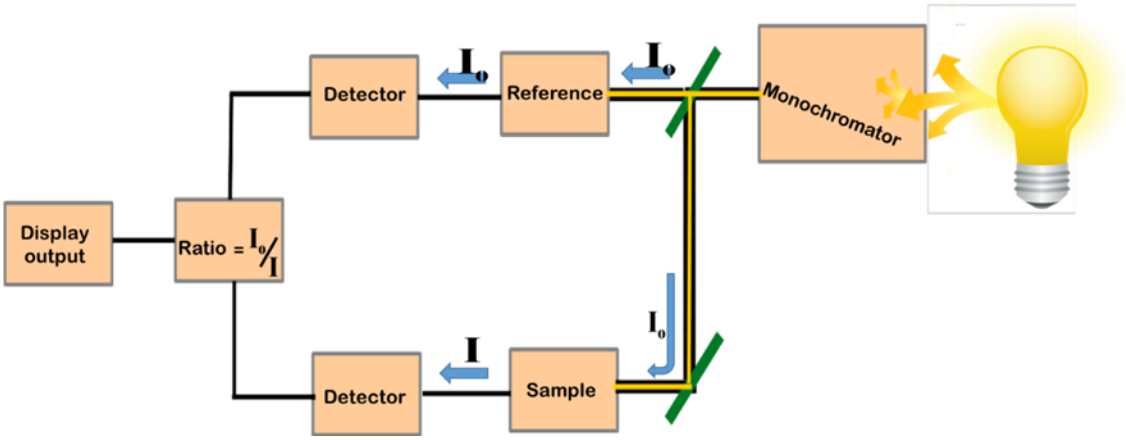

Figure 3.6: Schematic diagram of an optical absorption measurement using a monochromatic-beam UV-Visible Spectrometer.

A Tauc-plot (*Figure 3.7(b)*) derived from the Mott and Davis formula (*Equation 3.7*) is one method of determining the bandgap.

$$(\alpha h\nu)^{\frac{1}{n}} = A(h\nu - Eg) \qquad \text{Equation 3.7}$$

where *A* is a proportionality constant, *Eg* is bandgap, and *h* is the Plank constant, where α is the absorption coefficient, *h* is the Plank constant; *n* equals 1/2, 2, 3/2, and 3 for direct allowed, indirect allowed, direct forbidden, and indirect forbidden transitions, respectively. The Tauc-plot is a plot of the square of the product of the absorption coefficient and photon energy against photon energy for direct bandgap materials. As demonstrated in *Figure 3.7(b)*, the bandgap is the intercept on the energy axis of an extrapolation of the linear part of the graph. The link between the energy of a photon and wavelength in quantum mechanics, as shown in *Equation 3.8*, is another method used in this dissertation to determine the bandgap.

$$Eg\ (eV) = \frac{1240\ (eV.nm)}{\lambda(nm)} \qquad \text{Equation 3.8}$$

where *Eg* (eV) defines the bandgap and λ (nm) defines the wavelength of the photon at the onset of absorption as shown in *Figure 3.7(a).*

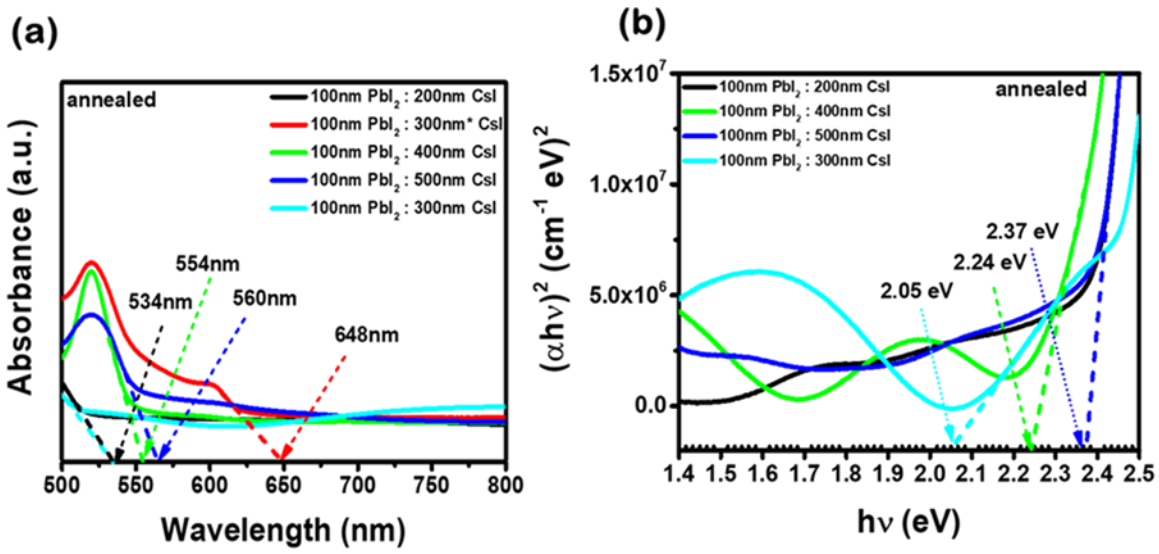

Figure 3.7: (a) $CsPbI_3$ optical absorption spectra for various PbI_2 and C thicknesses, (b) Direct bandgap Tauc's plot from $CsPbI_3$ optical absorption spectra for various PbI_2 and CsI thicknesses.

3.6 Device Characterization

3.6.1 Light current-voltage measurements

On the other hand, *Figure 3.8* shows conditions for standard illumination at room temperature for I-V measurements were carried out using a solar simulator system (Oriel LCS-100TM Small Area So11A Series, Oriel Cornerstone, Newport), a programmable voltage supply (Keithley 230), a source measure unit (SMU)(Key-sight B2912-A), and computer with Lab-VIEW Software. A built-in Xenon Arc Lamp (100 W), a mirror, and an AM1.5 filter made up the sun simulator. Moreover, the irradiance intensity of the simulator was calibrated using a standard cell (Oriel, model 91150V) linked to a thermocouple before the experiment begins. Light I-V measurements were conducted at 25 ℃ with a solar output of 1000 W/m^2 and AM1.5 G reference spectral filtering. After the dark measurements were completed, the bulb was switched automatically using LabVIEW Software to take the light measurements subsequently.

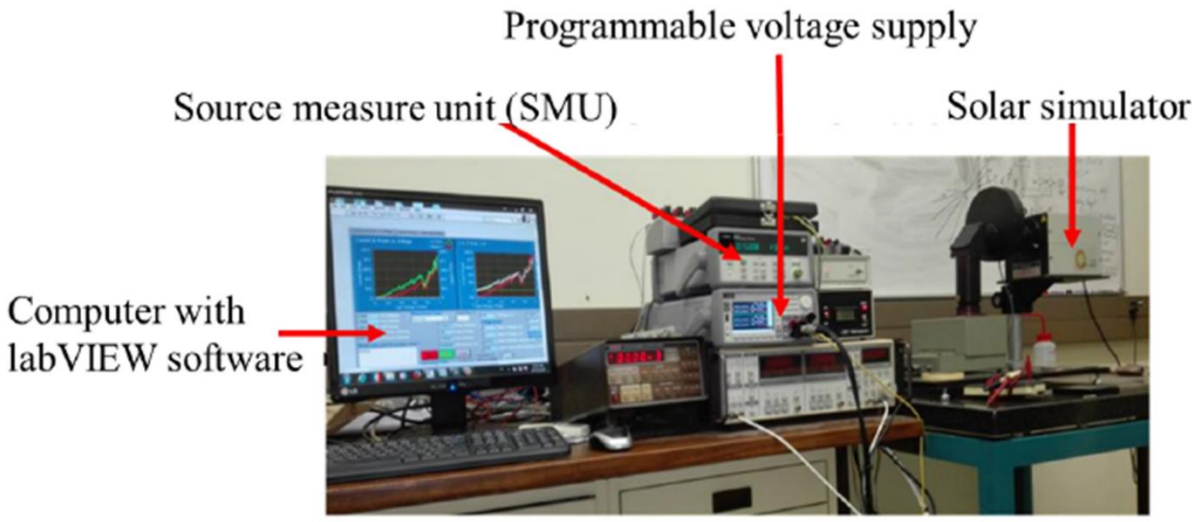

Figure 3.8: Standard illumination and dark automatic set-up for I-V measurements.

3.7 References

1. Muhammed Shafi, P. and A. Chandra Bose, *Impact of crystalline defects and size on X-ray line broadening: A phenomenological approach for tetragonal SnO_2 nanocrystals*. AIP Advances, 2015. **5**(5): p. 057137.
2. Ungar, T., *Microstructural parameters from X-ray diffraction peak broadening. Scripta Materialia*, 2004. **51**(8): p. 777-781.
3. Williamson, G. and W. Hall, *X-ray line broadening from filed aluminium and wolfram.* Acta metallurgica, 1953. **1**(1): p. 22-31.
4. Fru, J.N., N. Nombona, and M. Diale, *Synthesis and characterisation of methylammonium lead tri-bromide perovskites thin films by sequential physical vapor deposition*. Physica B: Condensed Matter, 2020. **578**: p. 411884.
5. <PhD_Dissertation_Fru-3.pdf>.
6. Mohammed, A. and A. Abdullah. Scanning electron microscopy (SEM): *A review. in Proceedings of the 2018 International Conference on Hydraulics and Pneumatics—HERVEX*, Băile Govora, Romania. 2018.

4 Results and Discussions

4.1 Introduction

This section describes the results of the pyrolysis of spray deposited compact titanium di-oxide (c-TiO_2). Furthermore, it presents the results of the synthesis of caesium lead tri-iodide ($CsPbI_3$) from lead (II) iodide (PbI_2) and various CsI thicknesses (single layers) using the sequential physical vapour deposition (SPVD) technique. In the end, it discusses the electrical properties of the fabricated FTO/TiO_2/$CsPbI_3$/Au device.

4.2 Spray pyrolysis deposition of titanium dioxide

4.2.1 Structural analysis for titanium dioxide properties

Figure 4.1 shows the XRD diffractograms of c-TiO_2 deposited on glass/FTO substrate using the spray pyrolysis (SP) technique. The XRD spectra of the film were measured using a Bruker D2-Phaser X-ray diffractometer using Cu Kα radiation at a wavelength of 0.15405 nm. Observed 2θ peaks of TiO_2 occurred at 26.53°, 33.76°, 37.76°, 51.53°, 54.57º, 61.58°, 65.55°, 77.33°, and 78.33°. Interestingly, these peaks are closely related to those of the polycrystalline anatase TiO_2 of the standard spectrum (JCPDS no.: 88-1175 and 84-1286). Identified peaks correspond to the crystallographic planes (101), (103), (004), (200), (105), (213), (116), (220), and (206), respectively. Furthermore, the orientation of the 2θ diffraction peaks at 26.53° and 37.75° corresponds to that of anatase phase material and is in good agreement with JCPDS 21-1272 file number. We were able to identify the crystal phase and estimate crystallite size from diffractogram measurements. Therefore, the main peak at 2θ = 26.53° matches the (101) crystallographic plane of the anatase phase for c-TiO_2 nanoparticles, indicating that the nanoparticles contributed only to the pure anatase phase, neither the rutile nor the brookite phase. The average computed crystallite size of c-TiO_2 was calculated using the well-known Debye-Scherrer's formula shown in *Equation 4.1*.

$$D = \frac{k\lambda}{\beta Cos\ \theta} \qquad \text{Equation 4.1}$$

where D = crystal Size (nm), β = full width at half maxima of the peak (FWHM) in radians, and λ = wavelength (1.5406 Å). The average crystal size was calculated and found to be 24.44 nm. The strain produced by crystal defects was analyzed by using a modified Williamson-Hall *Equation 3.3*. The average micro-strain was calculated as 9.75×10^{-4}.

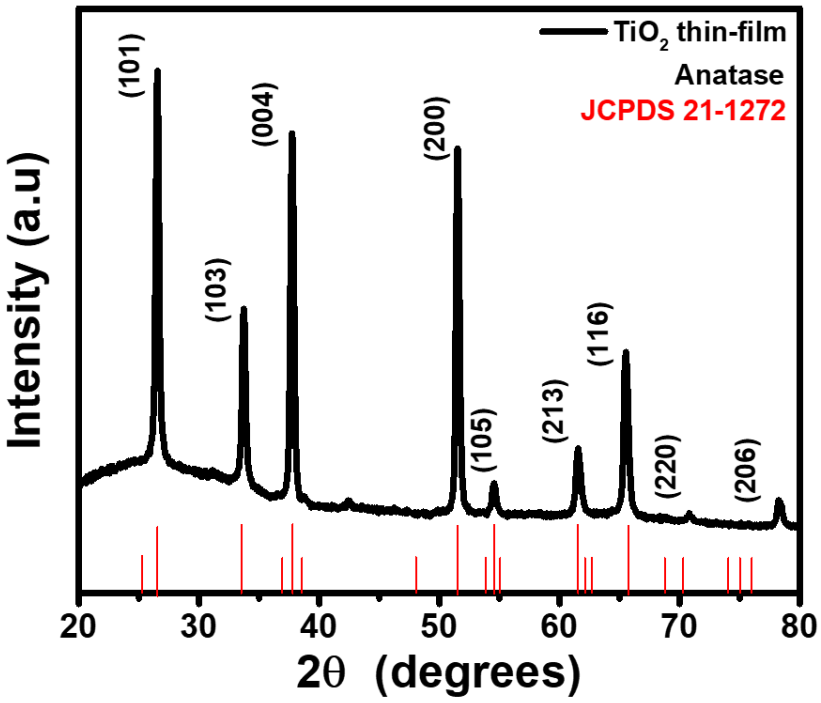

Figure 4.1: XRD pattern of c-TiO_2 thin film on FTO/glass substrate.

4.2.2 Titanium dioxide morphological properties

The morphology of the film was observed using field-emission scanning electron microscopy (FE-SEM). *Figure 4.2(a)* Illustrates agglomerated morphology on the top surface of the film [1]. *Figure 4.2(c)* shows full surface coverage of the substrate at small magnifications.

Additionally, nanoparticles displayed in *Figure 4.2(b)* are perfectly dispersed crystalline particles with a tetragonal crystal structure depicted by the XRD peak's broadening in *Figure 4.1*. However, the effect of the crystallinity materials on the broadening of the XRD patterns of nano-sized TiO_2 is negligible. The film crystal sizes range from 25 - 29 nm which are comparable to the mesoporous TiO_2 thin films reported by *Kim et al.* [2], with large pinhole-free surface topography. XRD diffractograms agree with the SEM micrographs revealing a homogeneity property with no residuals of impurities from the precursors. Therefore, it is seen that quality c-TiO_2 thin film was successfully synthesized.

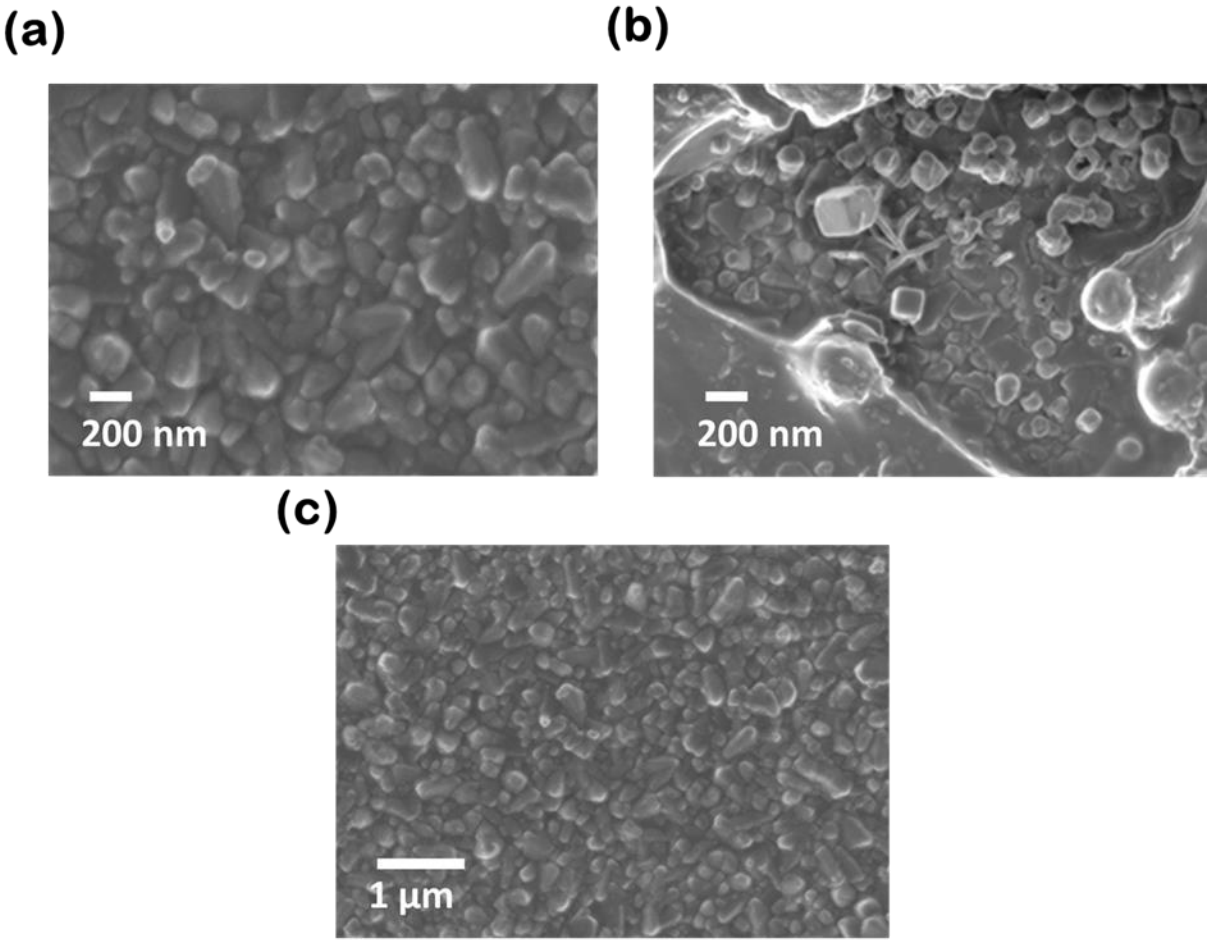

Figure 4.2: Top-view field-emission scanning electron microscopy (FE-SEM) images of TiO_2.

4.2.3 Titanium di-oxide optical properties

Figure 4.3(a) also shows the plot of absorbance vs. wavelength for the TiO_2 thin films prepared by the spray pyrolysis technique. Therefore, plotting the tangential line to the curve of the graph helps to obtain the absorption wavelength of the TiO_2 film (338 nm) as illustrated in *Figure 4.3(a)*. Using Einstein quantum photon energy according to *Equation 4.2*:

$$Eg = \frac{h\nu\ (eV.nm)}{\lambda\ (nm)} \qquad \text{Equation 4.2}$$

where E_g = bandgap (nm), $h\nu$ = 1240 (eV.nm) photon constant, and λ = measured wavelength (nm) the optical bandgap of the c-TiO_2 film was estimated to be 3.9 eV as shown in *Figure 4.3(b)*. The wide bandgap confirms the translucency of c-TiO_2 thin-film, as well as the material's ability to absorb in the IR region.

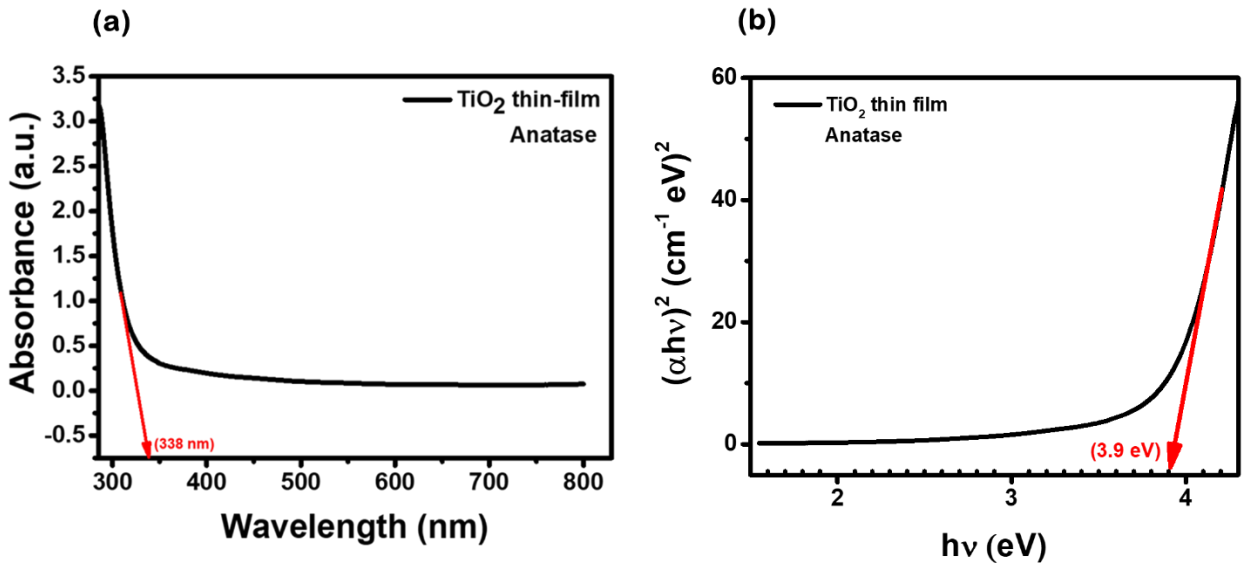

Figure 4.3: (a) Absorbance and, (b) Tauc plot for the bandgap estimation of TiO_2 thin film.

4.3 Sequential physical vapor deposition of caesium lead tri-iodide

4.3.1 Structural analysis for caesium lead tri-iodide

In *Figure 4.4*, diffractograms of 3D $CsPbI_3$ thin films for varying CsI thicknesses on FTO are shown. Diffraction directions at 26.69°, 33.67°, 37.71°, and 51.58° appear to correspond to (110), (101), (200), and (211) planes in FTO peaks [3a]. The increased peak intensities occurring at 2θ = 26.69° and 37.71°, suggest that the FTO peaks match that of $CsPbI_3$, resulting in the most intense diffractograms. Sharp peak patterns are observed from Bragg's diffractograms, indicating good crystallinity. $CsPbI_3$ measured 2θ peaks occurred at 12.92°, 21.04°, 22.88°, 26.69°, 27.84°, 33.67°, 37.91°, 41.66°, 46.01°, and 51.69°. These peaks closely match the peaks of the polycrystalline orthorhombic $CsPbI_3$ corresponding to JCPDS card file no 741970. These peaks correspond to the crystallographic planes (001), (111), (112), (121), (122), (101), (132), (200), (117), (114), and (211), respectively. The extra peak footprints observed in the orthorhombic polycrystalline patterns are evidence of PbI_2 observed at 12.92° with the crystallographic plane (001), initially indexed by JCPDS card no 7-0235, and supported by the XRD spectrum of the PbI_2 powder reported by *Zhao et al.* [3b]. But its intensity is seen to decrease with the increase in CsI thickness. This could be due to the decrease in the number of carbon, hydrogen, and bromine atoms at the Wyckoff positions of the space group, resulting in a low structure factor and thus the depleted-intensity peaks as CsI (500nm) thickness for both as-deposited and annealed films, could be due to a decrease in the number of carbon, hydrogen, and iodine atoms at the Wyckoff positions of the space group. Further, as CsI thickness was increased, the orientation of planes in given directions decreased, lowering the multiplicity factor and thus peak intensities. The $CsPbI_3$ peak positions also show the structure and symmetry of the contributing phase. Calculated lattice constants closely match the yellow optically active γ-$CsPbI_3$ perovskite thin films with JCPDS card file no 741970, showing crystal structures of the orthorhombic phase with a = 4. 88 Å, b = 9.96 Å, and c = 16.52 Å. *Figure 4.4(a)* illustrates the crystallization of $CsPbI_3$ for as-deposited films to reveal the orthorhombic crystal structure on the onset deposition inside the chamber. Because the temperature of the substrate was 190 ℃ during the evaporation of the CsI on PbI_2, simultaneous crystallization within the chamber occurred. This temperature is significantly low to the literature's

annealing temperature (330 ℃) for the orthorhombic $CsPbI_3$ [3]. Due to the thermodynamic energy generated during the evaporation process, CsI diffused into the gaps in the PbI_2 octahedral framework, resulting in the formation of $CsPbI_3$. Thus, only a brief time (less than 10 minutes) of post-annealing 100 ℃ was suitable to improve the crystallization of orthorhombic $CsPbI_3$ while maintaining good crystallinity.

A W-H plot was used to estimate the contribution of crystallite size and micro-strain to line broadening in *Figure 4.4(c).* Since the micro-strain and crystallite sizes are equal to a constant multiplied by the reciprocal of the intercept, which correlates with the W-H plot ($FWHM\cos(\Theta)$ vs. $4\sin(\Theta)$) of the $CsPbI_3$ diffractogram shown in *Figure 4.6*. It is seen that a positive slope indicates the positive micro-strains which may be the result of compressive stress, stacking faults, and the fact that strain is not the main cause of peak broadening. Also indicates that the origin of the micro-strain is from thermal annealing; thus minimizing the interface, surface, and grain boundary energies in the course of grain growth. Therefore, the SPVD process is likely to induce tensile or compressive stress on the substrates due to particle bombardment. As the thickness of CsI rose, the magnitude of the micro-strain showed an increasing trend, as illustrated in *Figure 4.5(a)*. The magnitude of micro-strain affects the degree of lattice distortion, which is defined by the change in a lattice constant from its bulk value. Calculated lattice constants from the peak's broadening of the XRD revealed good agreement of the yellow optically active γ-$CsPbI_3$ perovskite films [4], displaying crystal structures of the orthorhombic phase with a = 4. 88 Å, b = 9.96 Å, and c = 16.52 Å parameters. *Figure 4.4(c)* shows the crystallite sizes of $CsPbI_3$ thin films for various CsI thicknesses. CsI thickness increases with crystal size, according to a study. The increase in average crystallite size with the thickness of CsI could be due to some degree of increase in the size of the compressive micro-strain shown in *Figure 4.5(a).*

The variation of dislocation density with CsI thickness is seen in *Figure 4.4(d)*. The dislocation density was observed to increase from $6.17\text{x}10^{-9}$ to $1.69\text{x}10^{-9}$ cm^{-2} as the thickness of CsI is increased. *Hyder and Wilkov* [5] revealed that the effect of dislocation density has a negative impact on the Voc, Isc, PCE, and minority carrier lifetime of Indium gallium nitride (InGaN)-based multi-junction solar cells. Which explains a similar effect for the film at 400 nm CsI

thickness. The film could follow the same trend with the smallest dislocation density trend resulting in a high PCE device (see *Table 4.1.*

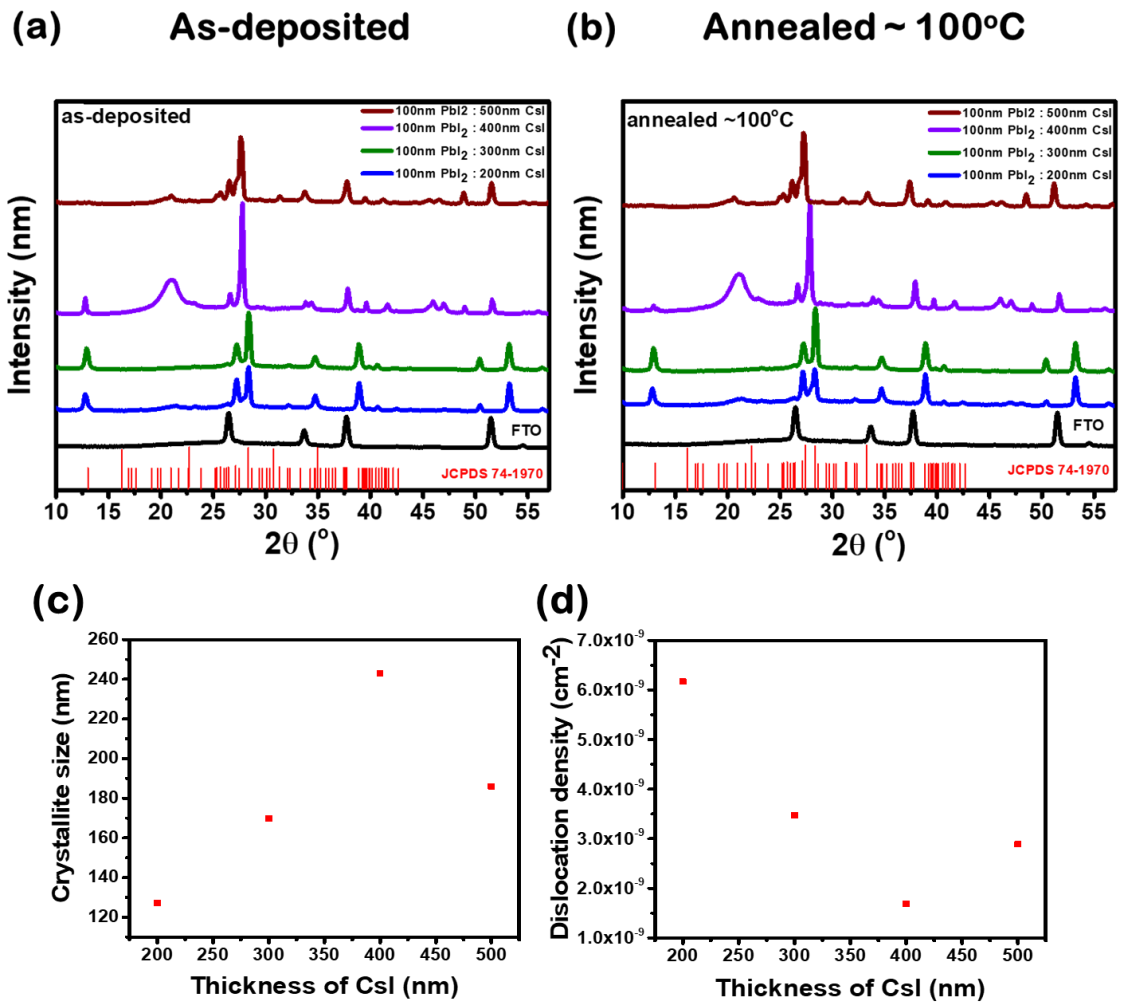

Figure 4.4: W-H plot (FWHMcos (Θ) vs. 4sin (Θ)) of the $CsPbI_3$ diffractogram.

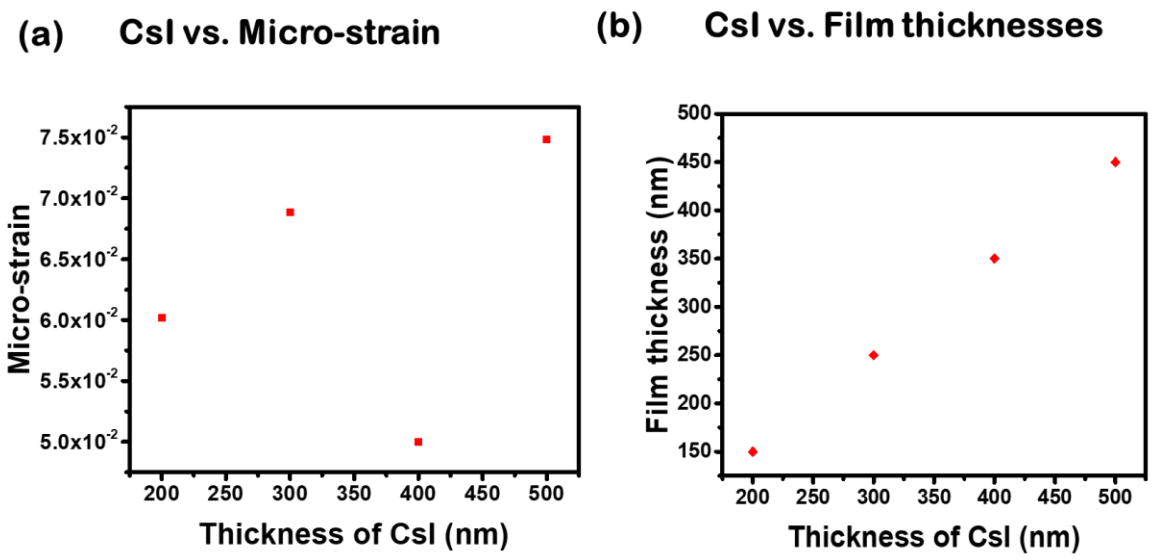

Figure 4.5: Illustration of (a) CsI vs. Micro-stain and (b) CsI vs. Film thickness.

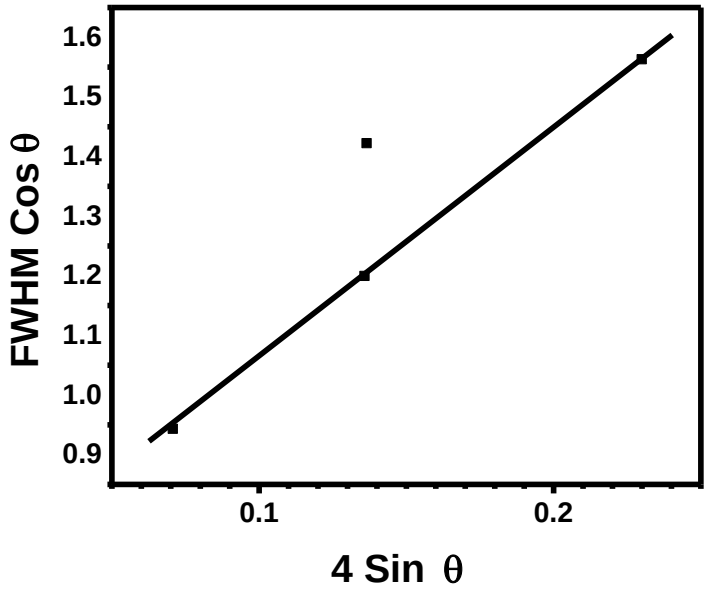

Figure 4.6: W-H plot (FWHMcos (Θ) vs. 4sin (Θ)) of the $CsPbI_3$ thin film's diffractograms.

4.3.2 Caesium lead tri-iodide morphological properties

The top-view SEM images of $CsPbI_3$ thin films in *Figure 4.7* and *Figure 4.8* resolve closely packed assemblies of discrete crystalline nanoparticles for the films, regardless of the variation of CsI thickness for both as-deposited and post-treatment (annealed films). This indicates that the film morphology is retained for various CsI thicknesses. Both annealed and as-deposited films for various CsI thicknesses exhibit similar surface morphology, demonstrating that access to CsI precursors has a negligible impact on the grain growth of the $CsPbI_3$ films. In addition, the influence of deposition rate on the surface morphology of $CsPbI_3$ nanoparticles films shows a negligible effect as examined using field-emission scanning electron microscopy (FE-SEM). The micrographs in *Figure 4.7* and *Figure 4.8* show that as-deposited and annealed (100 ℃) thin films are composed of 3D with non-uniform particle size. Furthermore, *Figure 4.9* shows the average grain size diameter and length for both as-deposited and post-treated films to vary from 170 nm to 240 nm and 160 nm to 240 nm respectively. In addition, the particle's grain variation confirms the polycrystallinity of the film [6]. Moreover, these difference in orientation and grain sizes during film growth is a result of the competition to minimize grain boundary, stain energies [7], interface, and maximize surface coverage. There are no pinholes in the grains and they are tightly packed. The grain orientation of this nature retains an advantage in the application of solar cells because it reduces photocurrent leakage and minimizes recombinations through shunt paths [8]. The results of *Eperon et al.* [9] show that high photocurrent and PCE can be achieved through full substrate coverage substrate thin films.

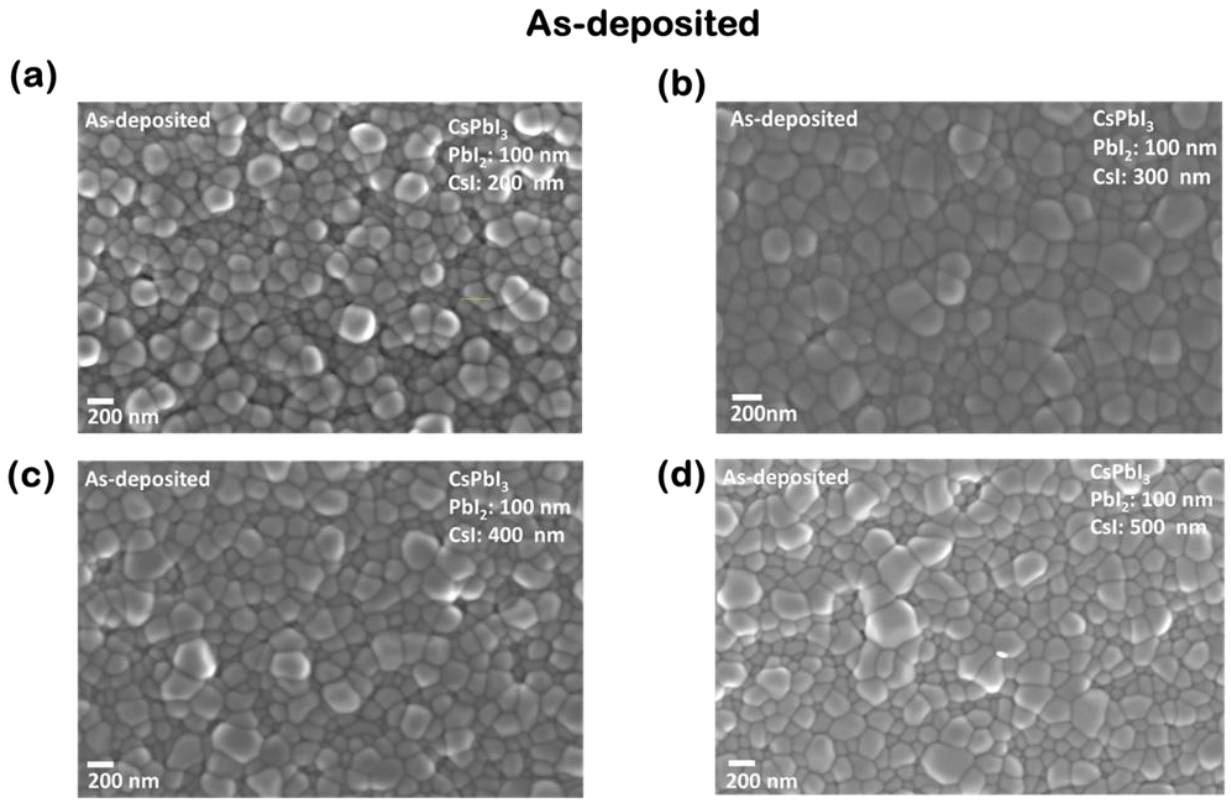

Figure 4.7: Top-view field-emission scanning electron microscopy (FE-SEM) images of $CsPbI_3$ layer with varying CsI thickness (a) 200 nm, (b) 300 nm, (c) 400 nm, and (d) 500 nm for as-deposited.

Fru et al. [10] report a sequential process for vapor deposition for achieving smooth film quality and uniform coverage. Annealed samples from 0 to 10 min intervals retained negligible effects on the surface morphology. However, annealing time played a vital role in the effective intercalation of CsI and PbI_2 to produce a perfect transformation of $CsPbI_3$ surface morphology [11]. Based on the FE-SEM micrographs shown in *Figure 4.7(a-d)-Figure 4.8(a-d)* the grain sizes contribute to the perfect surface morphology of $CsPbI_3$. Also minimizing possible abnormalities and dislocation effects during grain growth. The results show a subsequent increase in grain size from 300 nm to 500 nm for both as-deposited and annealed films as CsI thickness increases. The extended deposition time in the chamber could result in a reduction in the average grain size. Also, the imbalance of the precursor's ratios has a negligible effect on the film's morphology. In addition, *Figure 4.8(a)* and *(b)* shows that the SEM micrographs have a negligible effect on the morphology as the PbI_2 peak diminish with an increase of CsI thickness according to the XRD plots in

Figure 4.4(a) and *(b)*, confirming no PbI_2 residuals upon $CsPbI_3$ formation. Therefore, grains at 300 nm CsI thickness have compact and relatively large average grain sizes as shown in *Figure 4.8 (b)*. The compactness of these pin-hole free grains suppresses the grain boundaries and as a result, the film is expected to show high absorption coefficients [12]. Absorption by a film is very likely to be determined by the quality of its morphology. Therefore, it is noteworthy that the sample possesses attributes of a good absorbing thin film. Contrary, the film (300 nm CsI thickness) could be subjected to current leaks due to the relatively large grains (~240 nm shown in *Figure 4.9*) activating extended grain boundaries. Besides, *Lau et al.* [13] showed that quality morphology is an ideal tool for good contact between the active layer and the HTL, leading to improved device performance.

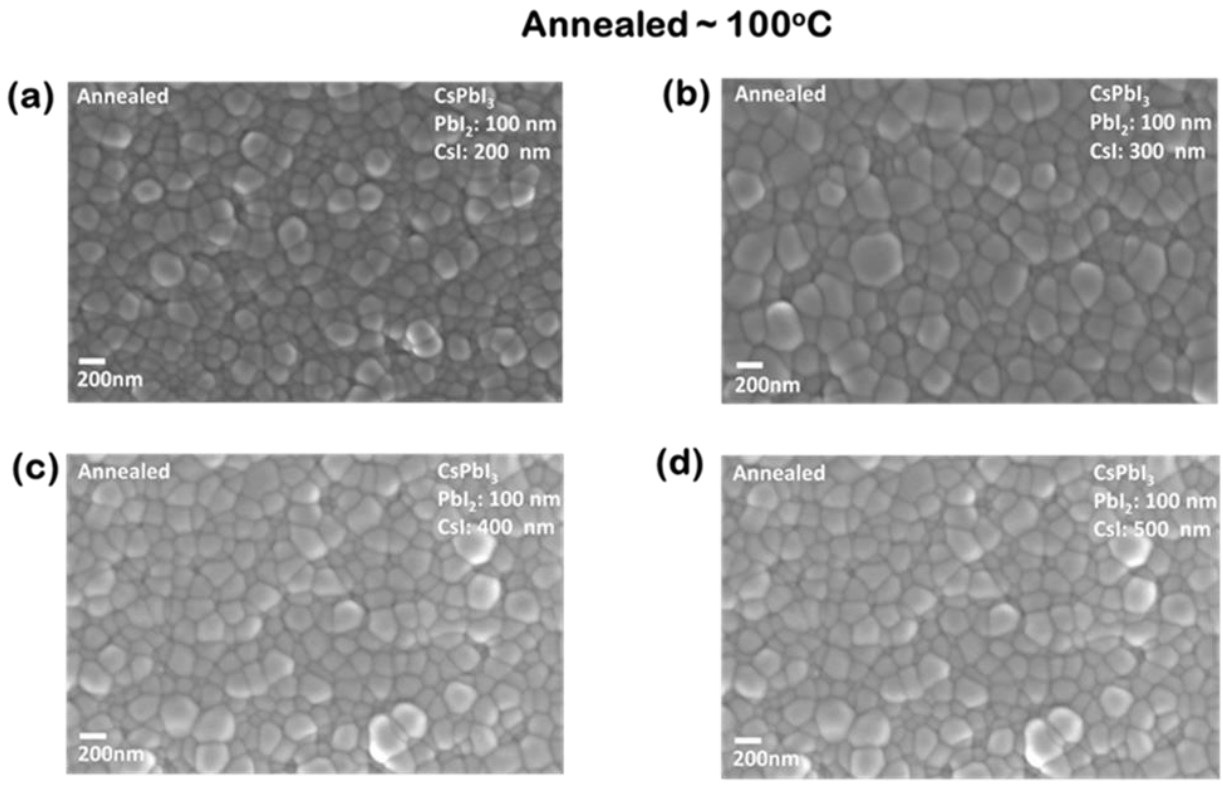

Figure 4.8: Top-view FE-SEM images of $CsPbI_3$ layer with varying CsI thickness (a) 200 nm, (b) 300 nm, (c) 400 nm, and (d) 500 nm for annealed (100 ℃) samples.

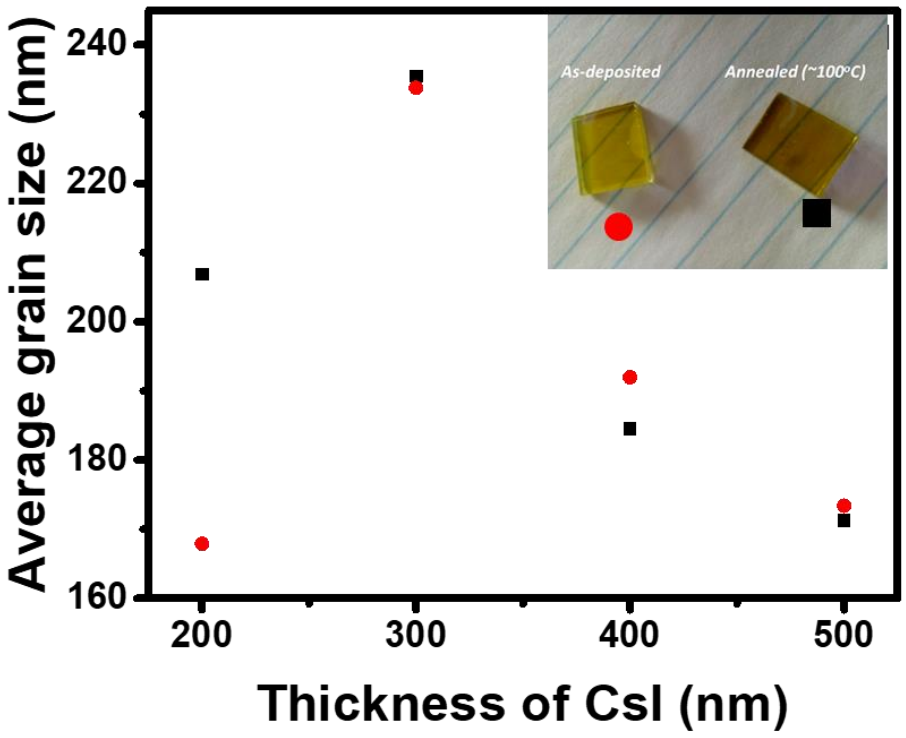

Figure 4.9: Distribution of $CsPbI_3$ average grain size (nm) with varying CsI thickness (from 200 nm – 400 nm) in steps of 100 for depicted as-deposited and annealed samples.

4.3.3 Caesium lead tri-iodide optical properties

Figure 4.10(a) and *(b)* shows the absorbance vs. wavelengths plots for the fabricated $CsPbI_3$ for varying CsI thicknesses. The thin films reveal absorptions in the range between 500 nm – 600 nm. *Figure 4.10(a)* shows a decreasing wavelength as CsI is increasing from 200 nm – to 500 nm for as-deposited $CsPbI_3$ films. Also, *Figure 4.10(b)* illustrates a similar consistent trend for a decrease in wavelength as CsI thickness increases. Furthermore, *Figure 4.10(c)* and *(d)* show the Tauc's plots of $CsPbI_3$ perovskite thin films prepared on FTO substrates with varying CsI thicknesses. It is evident from *Figure 4.11(c)* that $CsPbI_3$ films that have been post-treated (at 100 °C for 10 minutes) have better absorption, with the smallest bandgaps starting at 2.05 eV and the largest at 2.37 eV. A high-quality perovskite with fewer or no pinholes is beneficial for absorbing more light. Therefore, the small bandgap from the 300 nm CsI sample post-annealing shows

attributes of good light absorption with consistent discussion based on the SEM micrographs shown in *Figure 4.7(a-d)*. Additionally, Tauc-plot calculations have indicated that the bandgap in the as-deposited perovskites increased from 2.28 eV to 2.38 eV as the CsI thickness increased from 200 nm to 500 nm. Calculated bandgaps are consistent with the reported bandgap in literature for the most stable (orthorhombic polymorph) $CsPbI_3$ [15]. The large bandgaps of this type are believed to be the result of the common octahedral tilting phenomena: in organic-inorganic hybrid perovskites, similar octahedral tilting [16] and corresponding bandgap increases were also widely observed [17]. Metal-halide orbital overlap is reduced as a result of the described phenomenon, where moving the valence band to lower energies increases the bandgap [16]. However, because the δ-phase is not a perovskite, other factors, such as octahedra edge-sharing, may play a role in defining the bandgap.

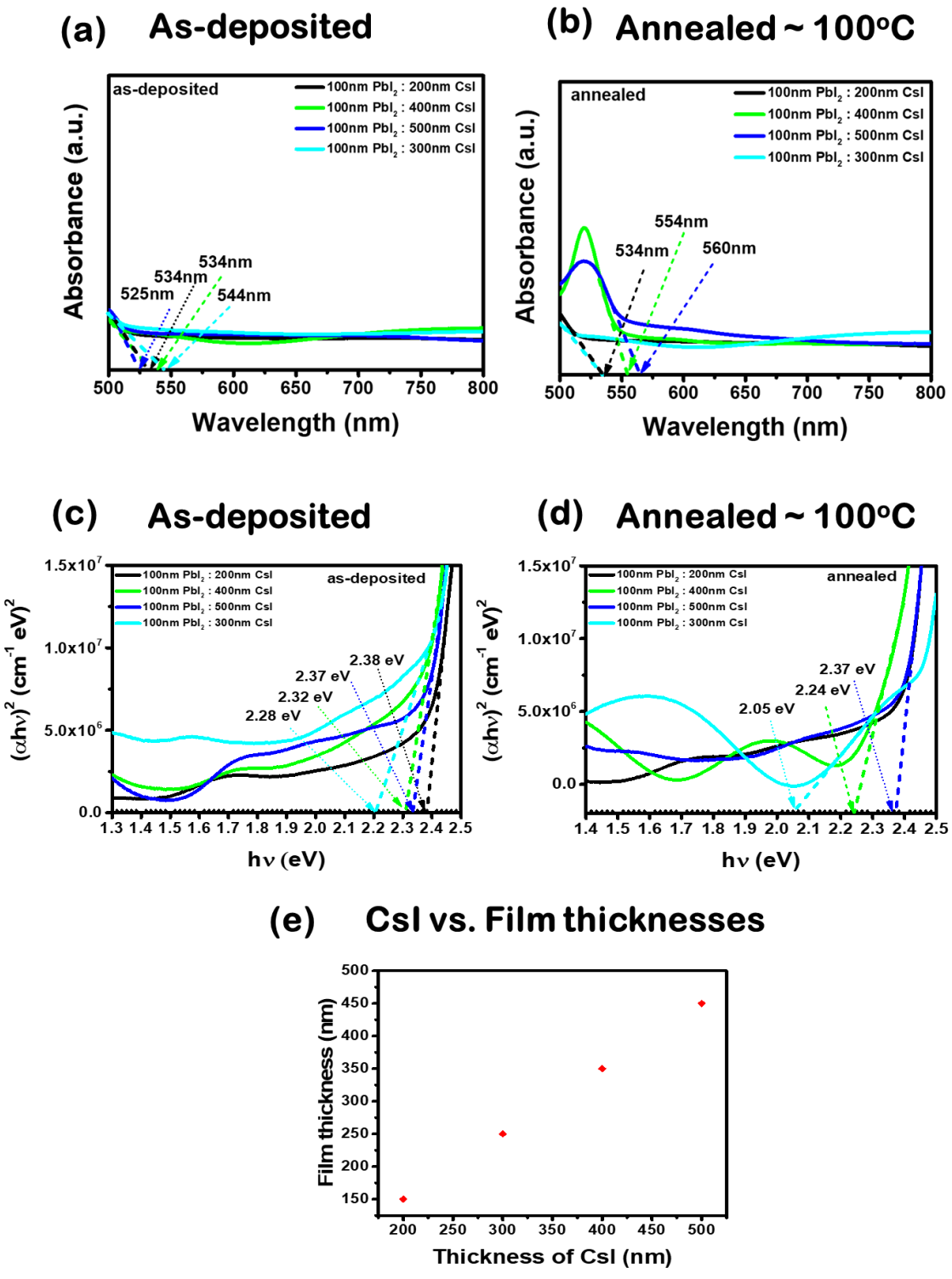

Figure 4.10: Absorbance's plots for (a) as-deposited (varying 200 nm – 500 nm CsI thickness), annealed 100 °C (varying 200 nm – 500 nm CsI thickness) the fabricated $CsPbI_3$ thin films. Tauc's plot for determining the bandgaps of $CsPbI_3$ layer deposited with different CsI thicknesses for (c)

as-deposited (200 nm – 500 nm) and (d) annealed 100 °C (200 nm – 500 nm). (e) The film thickness of $CsPbI_3$ vs. Thickness of CsI.

4.4 Photovoltaic performance of HTL free FTO/TiO_2/$CsPbI_3$/Au devices

4.4.1 Current-voltage analysis of Au/$CsPbI_3$/TiO_2/FTO devices under illumination

The photovoltaic performance of the $CsPbI_3$ perovskite solar cells (PSCs) fabricated is confirmed for various CsI thicknesses. All photovoltaic parameters, including open-circuit voltage (Voc), short-circuit current density (Jsc), fill factor (FF), and power conversion efficiency (PCE), for the fabricated $CsPbI_3$-based devices, are shown in *Table 4.1.*

Table 4.1. *Photovoltaic parameters of a light current-voltage (I-V) measurements for $CsPbI_3$ solar cells with different thicknesses CsI.*

CsI Thickness (nm)	V_{OC} (V)	J_{SC} (mA/cm^{-2})	Rsh (Ω/cm^{-2})	Rs (Ω/cm^{-2})	FF (%)	PCE (%)
200	0.96	17.29	91070.25	42496.66	26.85	4.49
300	0.27	20.40	15402.53	10294.93	28.05	1.53
400	0.88	10.89	888333.00	31718.28	41.98	4.04
500	0.75	18.66	107117.80	22691.65	36.24	4.93

The 300 nm thickness FTO/TiO_2/$CsPbI_3$/Au solar cell generated up to a maximum of 20.40 mA/cm^{-2} Jsc from a small 0.27V, contrary to the 200 nm thickness FTO/TiO_2/$CsPbI_3$/Au solar cell a less current density 17.29 mA/cm^{-2} from a good Voc 0.96V. The aforementioned opposition could be a result of the current leakage (for 300 nm CsI thickness film) attributed to the relatively large average grain size of ~240 nm (in *Figure 4.9*). Furthermore, *Figure 4.11(a)* shows a device's performance with a PCE of 4.49% attributed to the good Voc. This efficiency as a result of the good Voc shows a small FF (26.85%) which is subject to imperfect shunt (Rsh) and series (Rs)

resistances, and possibly non-optimal interface contacts causing the s-shape of the scan as illustrated in *Figure 4.11(a).* Higher Rsh attenuates the Jsc, influencing the current leakage. Following Ohm's law, the leakage current through Rsh can be expressed as in *Equation 4.3*:

$$\text{Jsh} = \frac{V - JRs}{Rsh} \qquad \text{Equation 4.3}$$

Therefore, 400nm CsI thickness in *Table 4.1.* (with electronic device performance showing a better 41.98% FF is illustrated in *Figure 4.11(c)*), the device shows a reduced Jsc (10.89mA) which indicates the effect of the high Rsh at operating regime (0.88V Voc). The reduced light current is speculated to be the result of leakage current flowing opposite to the photocurrent in the device. The CsI thickness variation is also reflected in the fact that devices with 400 nm, 500 nm, and even 300 nm CsI thicknesses show consistent PCEs over 4%, while the 300 nm device (shown *in Figure 4.11(b)*) deviates to less than 4%. This inconsistency could be the result of multiple recombination loss mechanisms discussed by *Proctor et al.* [17]. Moreover, the device might have endured continuous device degradation as a result of lattice distortion (since the orthorhombic $CsPbI_3$ metastable phase is prone to phase transition to the stable non-active yellow phase at 25 ℃ room temperature (RT)). Finally *Figure 4.11(d)* shows the J-V scan for the 100 nm PbI_2 : 500 nm CsI fabricated $CsPbI_3$-based device, which showed the highest performance with Voc of 0.73V, Jsc of 18.54 mA/cm^{-2}, FF of 36.24% and PCE of 4.93% under ambient air conditions.

The resulting highest efficiency (4.93%) for the bulky perovskite-based device could be due to the good crystallinity as an attribute of the SPVD technique used by *Fru et al.* [8] for the synthesis of $MAPbBr_3$ thin films through vacuum-assisted evaporation. The films showed a good crystallinity, negligible unit cell distortion, and interfacial accumulation of defects.

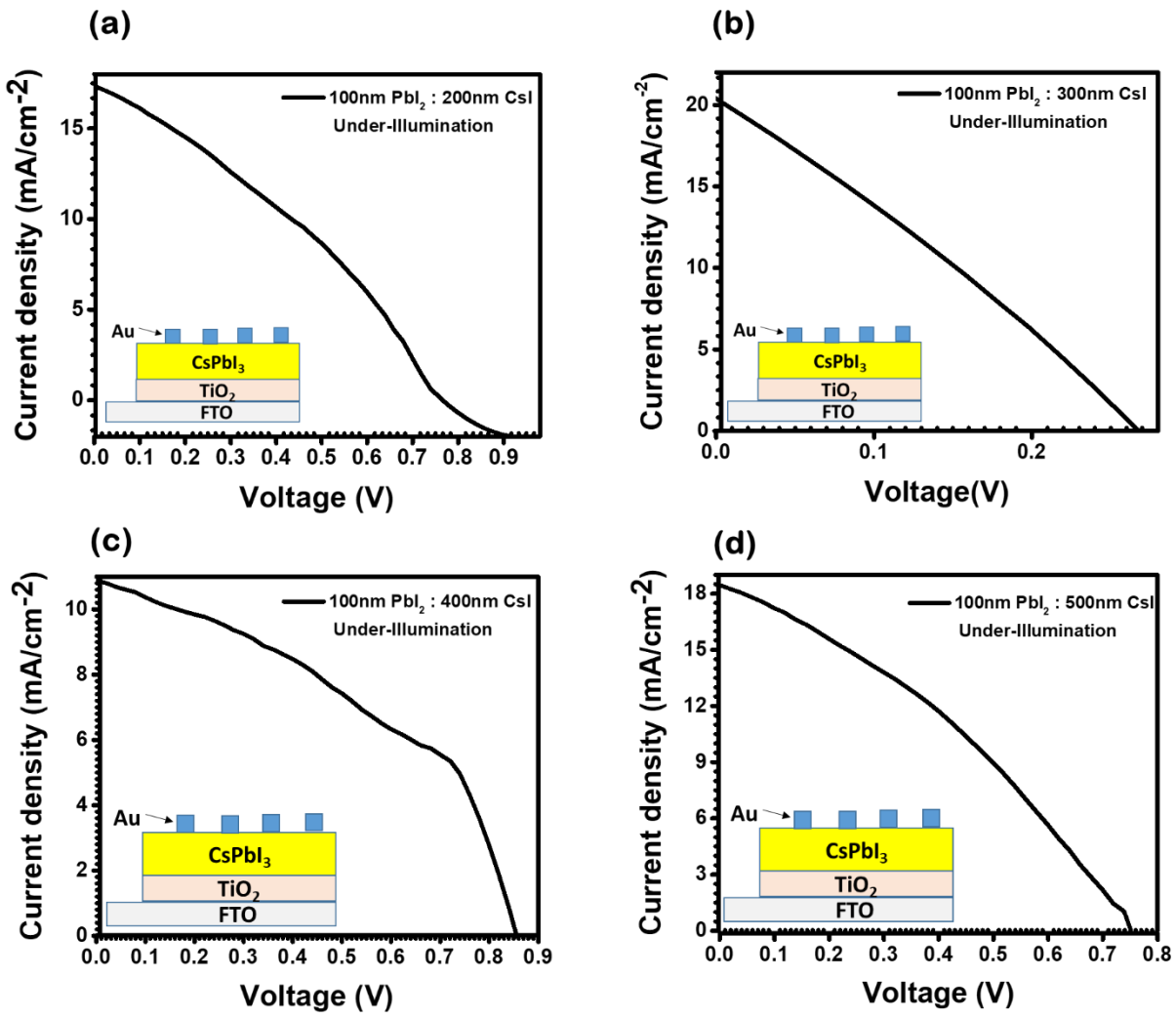

Figure 4.11: Electrical characterization of FTO/TiO_2/$CsPbI_3$/Au I-V characteristic at (a) 200nm CsI thickness, (b) 300nm CsI thickness, (c) 400nm CsI thickness, and (d) 500nm CsI thickness.

4.5 Conclusion

The above sections 4.1 – 4.4 outlines and provide a descriptive narrative on the structural, morphological, absorption spectra and I-V measurements for the deposited films of the solar cell's architecture (FTO/TiO_2/$CsPbI_3$/Au).

4.6 References

1. Zhou, D., et al., *Influence of material properties on TiO_2 nanoparticle agglomeration.* PloS one, 2013. **8**(11): p. e81239.
2. Kim, D.S., S.J. Han, and S.-Y. Kwak, *Synthesis and photocatalytic activity of mesoporous TiO_2 with the surface area, crystallite size, and pore size.* Journal of Colloid and Interface Science, 2007. **316**(1): p. 85-91.
3. (a) Mbulanga, C., et al., *Raman spectroscopy characterisation of oriented bundles of single-crystal rutile-phase TiO_2 nanorods prepared by hydrothermal bath deposition on transparent conducting substrates.* Applied Physics A, 2019. **125**. (b) Zhao, B., et al., *Thermodynamically stable orthorhombic γ-$CsPbI_3$ thin films for high-performance photovoltaics.* Journal of the American Chemical Society, 2018. **140**(37): p. 11716-11725.
4. Steele, J.A., et al., *Thermal unequilibrium of strained black $CsPbI_3$ thin films.* Science, 2019. **365**(6454): p. 679-684.
5. Hyder, S. and M. Wilkov, *Effect of Dislocation Density on the Epitaxial Growth of Silver.* Journal of Applied Physics, 1967. **38**(5): p. 2386-2387.
6. Thompson, C., *Grain growth in polycrystalline thin films of semiconductors.* Interface Science, 1998. **6**(1): p. 85-93.
7. Lee, D.N. and H.J. Lee, *Effect of stresses on the evolution of annealing textures in Cu and Al interconnects.* Journal of electronic materials, 2003. **32**(10): p. 1012-1022.
8. Fru, J.N., N. Nombona, and M. Diale, *Synthesis and characterisation of methylammonium lead tri-bromide perovskites thin films by sequential physical vapor deposition.* Physica B: Condensed Matter, 2020. **578**: p. 411884.
9. Eperon, G.E., et al., *Morphological control for high performance, solution-processed planar heterojunction perovskite solar cells.* Advanced Functional Materials, 2014. **24**(1): p. 151-157.
10. Fru, J.N., N. Nombona, and M. Diale, *Characterization of sequential physical vapor deposited methylammonium lead tri-iodide perovskite thin films.* Vacuum, 2020. **182**: p. 109727.

11. Yonezawa, K., et al., *Annealing effects on $CsPbI_3$-based planar heterojunction perovskite solar cells formed by vacuum deposition method.* Japanese Journal of Applied Physics, 2017. **56**(4S): p. 04CS11.
12. Jena, A.K., A. Kulkarni, and T. Miyasaka, *Halide perovskite photovoltaics: background, status, and future prospects.* Chemical reviews, 2019. **119**(5): p. 3036-3103.
13. Lau, C.F.J., et al., *Enhanced performance via partial lead replacement with calcium for a $CsPbI_3$ perovskite solar cell exceeding 13% power conversion efficiency.* Journal of Materials Chemistry A, 2018. **6**(14): p. 5580-5586.
14. Wang, B., N. Novendra, and A. Navrotsky, *Energetics, structures, and phase transitions of cubic and orthorhombic caesium lead iodide ($CsPbI_3$) polymorphs.* Journal of the American Chemical Society, 2019. **141**(37): p. 14501-14504.
15. Prasanna, R., et al., *Band gap tuning via lattice contraction and octahedral tilting in perovskite materials for photovoltaics.* Journal of the American Chemical Society, 2017. **139**(32): p. 11117-11124.
16. Lee, J.-H., et al., *Resolving the physical origin of octahedral tilting in halide perovskites.* Chemistry of Materials, 2016. **28**(12): p. 4259-4266.
17. Proctor, C.M., M. Kuik, and T.-Q. Nguyen, *Charge carrier recombination in organic solar cells.* Progress in Polymer Science, 2013. **38**(12): p. 1941-1960.

5 Conclusions and future work

5.1 Conclusions

In this study, we have used spray pyrolysis (SP), sequential physical vapour deposition (SPVD), and spin-coating as simple and reproducible techniques for growing high-quality c-TiO_2, 3D $CsPbI_3$ thin films for solar cells. The techniques helped to prepare high-purity TiO_2 electron transport layer (ETL), 3D $CsPbI_3$ absorbing layer (AL) thin films, respectively. 3D $CsPbI_3$ was perfected while varying CsI thickness. Variation of CsI thickness and annealing acquisition time (from 0 to 1 minute) played a fundamental role in optimizing the structure, morphology, and UV-Vis absorption of the completely inorganic 3D $CsPbI_3$ thin films. Additionally, the SPVD technique was applied to grow the $CsPbI_3$ films on glass/FTO and ITO substrates, and the degradation was observed for over a week on FTO.

Section 4.1 describes the growth of TiO_2 thin films deposited on glass/FTO using SPVD titanium tetraisopropoxide (TTIP) and ethanol solutions. The characteristics of TiO_2 including structural, morphological, and optical absorption of the film were discussed. XRD results revealed the tetragonal crystalline structure of c-TiO_2 with an anatase phase. The lattice constants, crystal size, and crystallinity were refined after post-treatment annealing at 450 ^oC. SEM micrographs showed amorphous compact surface topography of the film with full surface coverage. Additionally, the UV-Vis spectrum showed an estimated bandgap (3.64 eV) and good translucency of the electron transport film (c-TiO_2).

Section 4.2 reports directly on the growth of the 3D $CsPbI_3$ thin films on FTO using SPVD of PbI_2 and CsI single layer for the first time. An analysis of surface structure, morphology and optical absorption and photoelectrical properties of the 3D $CsPbI_3$ was presented and discussed as a

function of CsI thickness. Results based on the XRD diffractograms, when PbI_2 thickness was fixed at 100 nm and the CsI thickness was varied from 200 nm to 500 nm, the results revealed a tetragonal polycrystalline structure with an orthorhombic $CsPbI_3$ phase. The $CsPbI_3$ thin film's lattice constants, average crystal size, and crystallinity agree with CsI thicknesses for both as-deposited and annealed. Therefore, the decrease in the magnitude of compressive micro-strain was attributable to the increase in the average crystallite size and density of dislocations in the lattice structure. The average crystallite sizes at 200 nm and 300 nm CsI thick film were comparable and consistent with the theoretical observations of a stable γ-$CsPbI_3$ (at remarkably reduced dimensions ~100 nm [1]). Therefore, the thin films showed a negligible size distortion of the unit cell. Both as-deposited and annealed films presented similar attributes of the tetragonal polycrystalline structure of $CsPbI_3$, indicating that recrystallization of the orthorhombic $CsPbI_3$ thin film begins during PbI_2 and CsI deposition. During thermal evaporation of CsI, the substrate's temperature is elevated to 190 ℃, which is sufficient to induce CsI to diffuse into the voids of the PbI_6 octahedral framework, resulting in the formation of $CsPbI_3$. Additionally, as the CsI was increased from 200 nm to 500 nm, FE-SEM surface topography revealed pin-hole free and amorphously packed grains with an average size of 170 nm to 240 nm (for as-deposited films) and 160 nm to 240 nm (for annealed films). As average grain size grows, grain boundaries shrink, providing active areas for the accumulation of electron and hole traps that shorten charge carrier lifespan. The thin film's polycrystalline nature was further confirmed after 100 ℃ post-treatment (annealing temperature). UV-Vis absorbance was broad in the 500-600 wavelength range which is typical of γ-$CsPbI_3$. As the CsI thick was increased from 200 nm to 500 nm for as-deposited and annealed films, the bandgaps increased from 2.28 to 2.38 eV (as-deposited films), and 2.05 to 2.37 eV (annealed films). This demonstrated the fact that $CsPbI_3$ crystallization occurred within the deposition chamber and that post-deposition annealing has little effect on the optical characteristics of the sequential physical vapour deposited $CsPbI_3$.

Section 4.3 discussed the J-V plots obtained from the photovoltaics metrics studied using the I-V measurement system. Successfully fabricated FTO/TiO_2/$CsPbI_3$/Au devices revealed fluctuating PCEs ranging between 4%. On the other hand, the 300 nm CsI thickness sample showed a relatively low PCE that was caused by mechanical flaws, phase transition, prompt degradation, or primary recombination loss. Disregarding the cell's deviation which resulted in a small 0.27 V

Voc, it is safe to conclude that the Voc of FTO/TiO_2/$CsPbI_3$/Au devices increases with the reduction of CsI thicknesses (200 nm, 400 nm, and 500nm samples). In addition, the lower than 50% average FF leaves a void for further investigation into optimizing the devices.

5.2 Future work

The devices are functional, however, further work will be necessary to understand the limitations of these initial devices, and fabricate high-efficiency solar cells. On the prospects, we will look at factors including:

- **Adjusting the crystallization process**. Physical deposition possesses advantages, such as precisely controlling the thickness, optimizing the carrier lifetime, avoiding the limitations of precursor insolubility, and maintaining the morphology.
- **Improving the photophysical properties**. Following the guidance of *Wang et al.* [2] as he formed a channel for carrier transport and increased conductivity by using μ-graphene. Modify $CsPbI_3$ nanoparticle arrays by tuning the charge carries type and density for following the work of *Gaulding et al.* [3].
- Lastly, closely scrutinize the **annealing times**, and **temperatures**.

5.3 References

1. Zhao, B., et al., *Thermodynamically stable orthorhombic γ-$CsPbI_3$ thin films for high-performance photovoltaics.* Journal of the American Chemical Society, 2018. **140**(37): p. 11716-11725.
2. Wang, Q., et al., *μ-Graphene Crosslinked $CsPbI_3$ Quantum Dots for High-Efficiency Solar Cells with Much Improved Stability.* Advanced energy materials, 2018. **8**(22): p. 1800007.
3. Gaulding, E.A., et al., *Conductivity tuning via doping with electron-donating and withdrawing molecules in perovskite $CsPbI_3$ nanocrystal films.* Advanced Materials, 2019. **31**(27): p. 1902250.